

# Ultraviolet astronomical spectrograph calibration with laser frequency combs from nanophotonic lithium niobate waveguides

Markus Ludwig,<sup>1,\*</sup> Furkan Ayhan,<sup>2,\*</sup> Tobias M. Schmidt,<sup>3,\*</sup>

Thibault Wildi,<sup>1</sup> Thibault Voumard,<sup>1</sup> Roman Blum,<sup>4</sup> Zhichao Ye,<sup>5</sup> Fuchuan Lei,<sup>5</sup>

François Wildi,<sup>3</sup> Francesco Pepe,<sup>3</sup> Mahmoud A. Gaafar,<sup>1</sup> Ewelina Obrzud,<sup>4</sup> Davide Grassani,<sup>4</sup> Olivia Hefti,<sup>4</sup> Sylvain Karlen,<sup>4</sup> Steve Lecomte,<sup>4</sup> François Moreau,<sup>6</sup> Bruno Chazelas,<sup>3</sup> Rico Sottile,<sup>6</sup> Victor Torres-Company,<sup>5</sup> Victor Brasch,<sup>7</sup> Luis G. Villanueva,<sup>2</sup> François Bouchy,<sup>3</sup> Tobias Herr<sup>1,8,\*\*</sup>

<sup>1</sup>Deutsches Elektronen-Synchrotron DESY, Notkestr. 85, 22607 Hamburg, Germany

<sup>2</sup>École Polytechnique Fédérale de Lausanne (EPFL), 1015 Lausanne, Switzerland

<sup>3</sup>Observatoire de Genève, Département d’Astronomie, Université de Genève, Chemin Pegasi 51b, 1290 Versoix, Switzerland

<sup>4</sup>Swiss Center for Electronics and Microtechnology (CSEM), 2000 Neuchâtel, Switzerland

<sup>5</sup>Department of Microtechnology and Nanoscience, Chalmers University of Technology, 41296 Gothenburg, Sweden

<sup>6</sup>Observatoire de Haute-Provence, CNRS, Université d’Aix-Marseille, 04870 Saint-Michel-l’Observatoire, France

<sup>7</sup>Q.ANT GmbH, Handwerkstraße 29, 70565 Stuttgart, Germany

<sup>8</sup>Physics Department, Universität Hamburg UHH, Luruper Chaussee 149, 22607 Hamburg, Germany

\*These authors contributed equally.

\*\*tobias.herr@desy.de

**Astronomical precision spectroscopy underpins searches for life beyond Earth, direct observation of the expanding Universe and constraining the potential variability of physical constants across cosmological scales. Laser frequency combs can provide the critically required accurate and precise calibration to the astronomical spectrographs. For cosmological studies, extending the calibration with such *astrocombs* to the ultraviolet spectral range is highly desirable, however, strong material dispersion and large spectral separation from the established infrared laser oscillators have made this exceedingly challenging. Here, we demonstrate for the first time astronomical spectrograph calibrations with an astrocomb in the ultraviolet spectral range below 400 nm. This is accomplished via chip-integrated highly nonlinear photonics in periodically-poled, nano-fabricated lithium niobate waveguides in conjunction with a robust infrared electro-optic comb generator, as well as a chip-integrated microresonator comb. These results demonstrate a viable route towards astronomical precision spectroscopy in the ultraviolet and may contribute to unlocking the full potential of next generation ground- and future space-based astronomical instruments.**

Precise astronomical spectroscopy has led to the Nobel-Prize winning discovery of the first exo-planet via the *radial velocity method* [1], which relies on the precise tracking of minute Doppler-shifts in the stellar spectrum caused

by an orbiting planet. The detection of Earth-like planets in the habitable zone around a Sun-like star requires to measure a radial velocity change as small as 10 cm/s (relative Doppler-frequency shift of  $3 \times 10^{-10}$ ) over the time scale of 1 year. This necessitates regular wavelength calibration of the spectrograph against a suitable calibration light source. Highly stable and accurate calibration light sources hence take on a key role in astronomical precision spectroscopy.

Calibration sources with outstanding accuracy and precision can be provided by laser frequency combs [2, 3] (LFCs). Their spectra are comprised of large sets of discrete laser lines whose frequencies are precisely and absolutely known (linked to a metrological frequency standard including the SI second), on a level that exceeds the astronomical requirements. Provided their lines can be separated by the spectrograph, LFCs can serve as exquisite wavelength calibrators [4, 5] and are then also referred to as *astrocombs* (Fig. 1a). Recent years have seen significant progress in developing astrocombs [6–10] and extending their coverage to visible (VIS) wavelengths, where the emission of Sun-like stars peaks, and to near-infrared wavelength, where relatively cold stars can accommodate rocky planets in tight orbits.

Extending astrocombs further towards the atmospheric cutoff and into the ultraviolet (UV) regime would not only be relevant to exo-planet science, but highly desirable for fundamental physics and precision cosmology (Fig. 1b); indeed these are also major science drivers for the upcoming ANDES high-resolution spectrograph at the *Extremely*

*Large Telescope* (ELT) [11]. For instance, by accurately determining the wavelengths of narrow metal absorption features in the spectra of quasi-stellar objects (QSOs), one can infer the value of the fine-structure constant,  $\alpha$ , at the place and time of absorption, i.e. billions of years ago. This allows to test whether fundamental physical constants might have varied on cosmological scales [12, 13]. Another exciting, but extremely demanding science case is the direct observation of cosmic expansion in real time, often referred to as the *Sandage test* [14–16]. This requires detecting a drift of HI Ly $\alpha$  forest absorption features in QSO spectra by just a few cm/s (relative frequency shift of  $3 \times 10^{-11}$ ) over several decades. As lined out in [17], observations and corresponding wavelength calibrations in the UV are needed to access low redshifts,  $z$ , in particular the important zero-crossing of the drift at  $z = 2$ , corresponding to 365 nm (Fig. 1c). Achieving such an extreme level of wavelength stability will require a community effort over the next decade to develop improved spectrographs, data analysis methods, and in particular LFC-based calibration sources. Furthermore, it has recently become clear that a detailed modeling of the instrumental line-spread function is crucial to further improve accuracy and stability of spectroscopic observations [17–19]. This, however, requires a broadband calibration source with a spectrum of narrow lines, such as those of an LFC.

Astrocombs can be derived from high-repetition rate ( $f_{\text{rep}} > 10$  GHz) laser sources, such as line-filtered mode-locked lasers [6–8, 20], electro-optic (EO) comb generators [21, 22] and chip-integrated microresonators [23–27]. Their spectra consist of equidistant optical laser frequencies  $\nu_n = \nu_0 + n f_{\text{rep}}$ , spaced by the laser’s pulse repetition rate  $f_{\text{rep}}$  and with an offset frequency  $\nu_0$ , which we here define to be the central frequency of the laser ( $n$  is an integer comb line index). To transfer the comb spectra to the desired wavelength range and to increase their spectral coverage, second ( $\chi^{(2)}$ ) and third order ( $\chi^{(3)}$ ) nonlinear optical effects are utilized. However, the high repetition rates of  $> 10$  GHz, that are necessary for the comb lines to be separated by the spectrograph, imply low pulse energies and hamper nonlinear optical effects. In addition, and especially at shorter wavelengths, strong material dispersion complicates the efficient nonlinear energy transfer.

So far, short-wavelength blue and green astrocombs have been achieved via second harmonic generation of infrared mode-locked lasers [20, 29, 30] and of EO combs [31] in bulk  $\chi^{(2)}$ -nonlinear crystals. Spectral broadening in  $\chi^{(3)}$ -nonlinear photonic crystal fiber resulted in astrocombs spanning from infrared (IR) to VIS wavelength [32–34], some extending to below 450 nm. In addition to these approaches, micro- and nanophotonic waveguides made of highly nonlinear materials can further increase the efficiency in a compact setup. In the IR,  $\chi^{(3)}$ -nonlinear silicon nitride ( $\text{Si}_3\text{N}_4$ ) waveguides have led to broadband astrocombs [35], and via third harmonic generation a 10 GHz IR comb has been transferred to VIS wavelengths [36]. Strong nonlinear effects in waveguides, including harmonic fre-

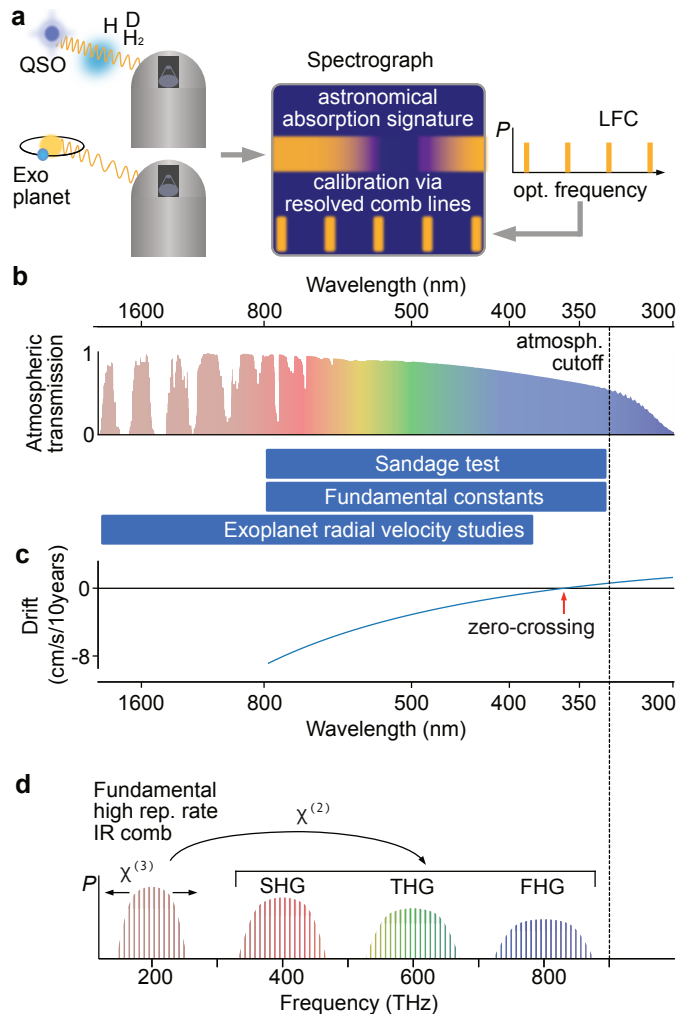


**Figure 1 | Ultraviolet astronomical precision spectroscopy.** **a**, Precision spectroscopy of astronomical objects enabled by laser frequency combs (LFC) providing absolutely and precisely known laser frequencies, cf. main text. QSO: quasi stellar object; H, H<sub>2</sub>: hydrogen; D: deuterium;  $P$ : optical power. **b**, Atmospheric transmission (high altitude, dry), spectral ranges for different astrophysical studies. **c**, Expected redshift drift signal for the standard  $\Lambda$ CDM cosmology [28] in units of cm/s per decade (Sandage test) as function of wavelength, corresponding to the redshifted HI Ly $\alpha$  transition. **d**, Concept of broadening and transferring a high-repetition rate astrocomb from infrared (IR) to visible (VIS) and ultraviolet (UV) wavelengths based on optical  $\chi^{(2)}$ - and  $\chi^{(3)}$ -nonlinearities.

quency generation, may also be obtained via the quadratic  $\chi^{(2)}$ -nonlinearity. At low pulse repetition rates, spectra across multiple optical octaves have been obtained in large-mode area ( $\sim 100 \mu\text{m}^2$ ) periodically poled lithium niobate ( $\text{LiNbO}_3$ ) waveguides with mm-long propagation distances [37–40]. Notably, periodically poled  $\text{LiNbO}_3$  waveguides were utilized with a 30 GHz repetition rate line-filtered erbium-doped mode-locked laser [41], creating harmonic spectra in VIS and UV domains for astronomical spectrograph calibration. In addition, recent work leveraged a combination of second harmonic and sum-frequency

generation based on a titanium-doped sapphire laser to obtain, in conjunction with line-filtering, a continuous green to ultraviolet 30 GHz astrocomb [42]. In nano-photonic waveguides from thin-film LiNbO<sub>3</sub>[43–48], owing to their sub- $\mu\text{m}^2$  modal confinement, highly efficient UV spectral generation has been reported [49–59], including at 10 GHz repetition rate [52]. However, astronomical spectrograph calibration in the UV spectral range has so far not been demonstrated.

Here, we demonstrate astronomical spectrograph calibration with laser frequency combs in the UV below 400 nm. Specifically, we design chip-integrated nano-structured LiNbO<sub>3</sub> waveguides with sub- $\mu\text{m}^2$  mode cross-section and a tailored poling-pattern to enable efficient UV astrocomb generation via cascaded harmonic generation from a robust telecommunication-wavelength 18 GHz EO comb, as well as, a 25 GHz chip-based microresonator comb. The generated astrocombs are tested in March 2023 on the high-resolution echelle spectrograph SOPHIE [60] at the Observatoire de Haute Provence (OHP, France), achieving radial-velocity precision in the range of 1 to 2  $\text{m s}^{-1}$ .

## Results

We base our astrocombs on a robust, telecommunication-grade EO comb with a pulse repetition rate of 18 GHz, as well as, a microresonator comb with a repetition rate of 25 GHz. Both are derived from an IR continuous-wave (CW) laser of frequency  $\nu_0 \approx 192$  THz (wavelength  $\approx 1.56$   $\mu\text{m}$ ) and operate intrinsically at high repetition rate, so that filtering of unwanted comb lines is not required. To transfer the IR comb to the UV (and VIS), we utilize chip-based LiNbO<sub>3</sub> nanophotonic waveguides, for cascaded harmonic generation as illustrated in Fig. 1d. The possible comb frequencies are

$$\nu_{m,n} = m\nu_0 + n f_{\text{rep}} \quad (1)$$

where  $m$  is the harmonic order. In general, each harmonic  $m$  of the comb spectrum has a different offset frequency  $m\nu_0$ . While this can facilitate detection of the comb’s offset frequency [50, 52, 54, 58], care must be taken to avoid inconsistent frequency combs from overlapping harmonics with different offsets. Alternatively, stabilizing  $\nu_0$  to a multiple of  $f_{\text{rep}}$  could address this point. Practically this could be achieved for instance by locking the beatnote between adjacent harmonics to zero [61], or via an auxiliary low-repetition rate frequency comb [62].

A key difference between broadband electro-optic combs obtained via conventional self-phase modulation  $\chi^{(3)}$ -based supercontinua and spectra generated via  $\chi^{(2)}$ -based harmonics, lies in the phase noise properties of their comb lines. In  $\chi^{(3)}$ -based spectra, the phase noise, impacting linewidth and line contrast, grows quadratically with the frequency distance from the fundamental pump laser. In contrast, in  $\chi^{(2)}$ -based harmonic spectra the phase noise (approximately) depends on the frequency distance from

it’s corresponding harmonic’s center frequency (see Supplementary Information SI, Section 1). This property, along with the efficiency of the nanophotonic waveguides, permits us to directly generate comb lines in the ultraviolet from a telecom-wavelength electro-optic source, within a certain bandwidth around the harmonic’s center frequency; future extension of this bandwidth will, as we discuss in detail in the Section 1 in the SI, require the addition of a noise filtering cavity, which has been established for broadband  $\chi^{(3)}$ -based electro-optic combs [63], but is not implemented in this initial proof-of-concept demonstration.

**Waveguide design.** An illustration of a nano-structured LiNbO<sub>3</sub> waveguide and the strong mode confinement to sub- $\mu\text{m}^2$  cross-section for efficient nonlinear conversion is shown in Figure 2a. The waveguides are fabricated from a commercially-available undoped lithium niobate-on-insulator (LNOI) substrate with an 800 nm-thick LiNbO<sub>3</sub> layer via electron-beam lithography and reactive-ion etching, resulting in a sidewall angle of  $\sim 75^\circ$  (Fig. 2c, Methods). The waveguides taper to a width of 2500 nm at the chip facet, for input and output coupling. In a first design step, considering the fundamental transverse electric polarization (TE) waveguide mode, we define the waveguide geometry, which in nano-photonic waveguides enables engineering of the waveguide’s group velocity dispersion (GVD), and additional  $\chi^{(3)}$ -nonlinear spectral broadening of the input IR comb. In unpoled waveguides, top widths in the range of 800 to 1200 nm result in anomalous GVD and the most significant broadening. Spectral broadening is also possible in the normal GVD regime, typically resulting in less broad, but more uniform spectra.

In a second design step, we define the waveguide’s poling pattern to transfer the broadened fundamental spectrum to shorter wavelengths. This can be achieved efficiently, when a fixed phase relation between the involved waves is maintained (*phase matching*). However, due to chromatic material dispersion, this cannot easily be fulfilled across the entire spectral interval of interest (regardless of the choice of waveguide geometry and GVD at the fundamental wavelength). As an alternative to natural phase matching, in ferroelectric crystals such as LiNbO<sub>3</sub>, *quasi-phase matching (QPM)* is possible. Here, the sign of the  $\chi^{(2)}$ -nonlinearity is periodically flipped within segments of length  $\Lambda$  (poling period), via poling of the crystal’s domains (Methods) to compensate the increasing phase-mismatch between the waves. For sum-frequency generation processes (which underlie harmonic generation),  $\Lambda$  is

$$\Lambda = 2\pi/|k_1 + k_2 - k_3| \quad (2)$$

where  $k_1$  and  $k_2$  are the input propagation constants, and  $k_3$  is the output propagation constant in the waveguide. To achieve broadband QPM,  $\Lambda$  may be chirped (i.e., varied along the waveguide). To design  $\Lambda(z)$  ( $z$  is the spatial coordinate in the propagation direction), we nu-

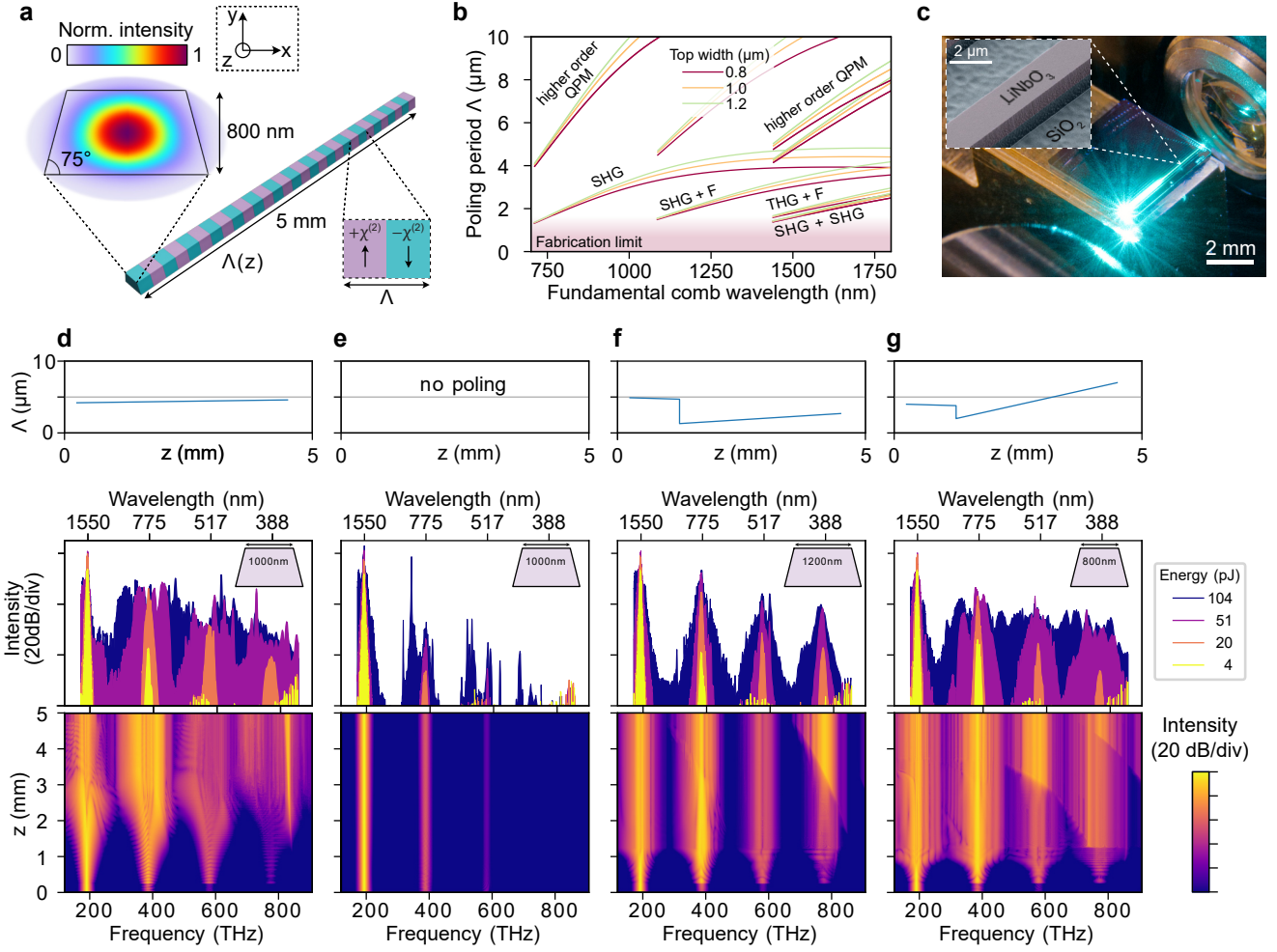


**Figure 2 | Nanophotonic lithium niobate waveguides.** **a**, Geometry of a nanophotonic lithium niobate ( $\text{LiNbO}_3$ ) waveguide, showing the optical mode profile for the fundamental transverse electric field (TE) mode and a possible poling pattern with spatially variable poling period  $\Lambda$ . The extraordinary crystal axis is oriented along the x-direction to access the highest electro-optic tensor element of  $\text{LiNbO}_3$ . **b**, Poling periods  $\Lambda$  required for quasi-phase matching of various nonlinear optical processes for waveguides of different (top) width as a function of the fundamental comb's wavelength. SHG: second harmonic generation; SHG + F: sum-frequency generation of second harmonic and fundamental comb; THG + F: sum-frequency generation of third harmonic and fundamental comb; SHG + SHG: sum-frequency generation of the second harmonic. Respective higher-order phase matching with three-fold period  $\Lambda$  is indicated (the current fabrication limit only allows for  $\Lambda > 2 \mu\text{m}$ ). **c**, Photograph of a waveguide in operation and scanning electron microscope image of the  $\text{LiNbO}_3$  on silica ( $\text{SiO}_2$ ). **d,e,f,g**, Examples of waveguide designs showing poling pattern (top), experimentally generated spectra for different input pulse energies provided by a 100 MHz, 80 fs mode-locked laser with central wavelength of 1560 nm (waveguide cross-section are shown as insets and on chip-pulse energy is indicated by the color code) and *pyChi* [64] simulation results (bottom) for a pulse energy of 50 pJ. The spurious spikes observed in the traces for 4 pJ pulse energy are manifestations of the noise floor of the optical spectrum analyzer (Yokogawa AQ6374).

merically compute the frequency  $\omega$  dependent propagation constants  $k(\omega)$  of the fundamental waveguide mode for waveguide top widths of 800, 1000 and 1200 nm. Based on Eq. 2, we derive the required poling period  $\Lambda$  for a number of sum-frequency processes that would result in second harmonic generation (SHG = fundamental+fundamental), third harmonic generation (THG = SHG+fundamental) and fourth harmonic generation (FHG = SHG+SHG or THG+fundamental). These periods  $\Lambda$  are shown in Fig. 2b, as a function of the fundamental comb's wavelengths.

Prior to astrocomb generation, we test different waveguide designs with a low-repetition rate (100 MHz), 80 fs mode-locked laser operating at a center wavelength of 1560 nm. The pulses are coupled to the chip via a high-numerical aperture lens (NA=0.7) lens and the spectra are collected using reflective collimation optics and a fluoride multimode fiber that connects to a grating-based optical spectrum analyzer (Yokogawa AQ6374). Utilizing a lensed fiber with a calibrated coupling efficiency as temporary output coupler, we determine the input coupling efficiency of the high-NA lens to be  $13 \pm 2\%$ . To illustrate the im-

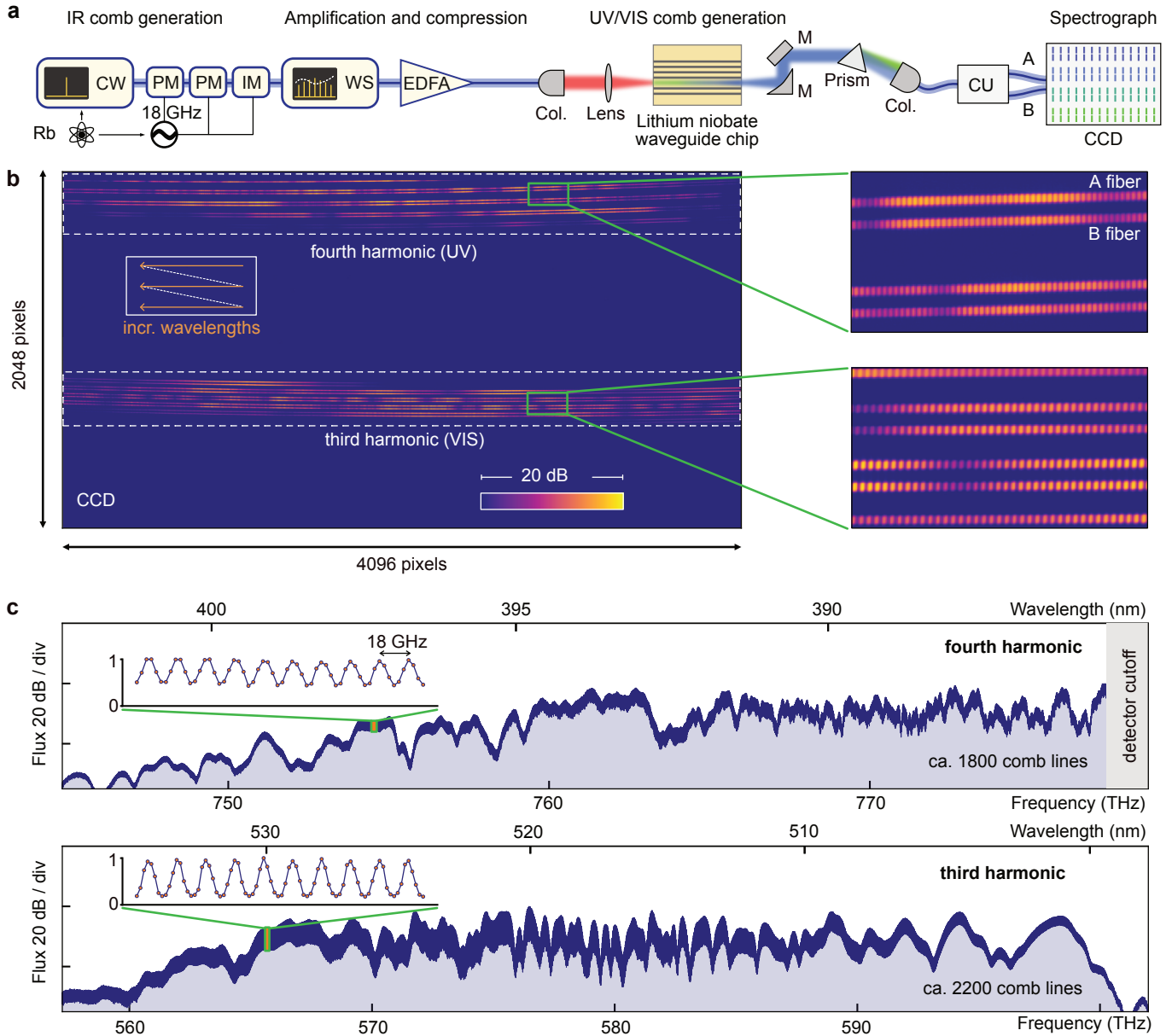


**Figure 3 | Ultraviolet astrocombs.** **a**, Setup for ultraviolet (UV) astrocomb generation. Rb: rubidium-based atomic references (cf. main text, Methods); CW: continuous-wave laser; PM: phase modulator; IM: intensity modulator; WS: wavershaper; EDFA: erbium-doped fiber amplifier; Col.: fiber-to-free-space collimator; M: mirror; CU: calibration unit splitting the comb equally into A and B fibers; CCD: SOPHIE charged coupled device detector. All fibers following the lithium niobate chip and feeding the spectrograph are multi-mode fibers. **b**, Composite CCD detector image, obtained with two different settings of the flux-balancing prism, showing fourth and third harmonic in the UV and visible (VIS) wavelength ranges. The inset indicates how wavelengths increase along the individual cross-dispersed echelle orders. The magnified CCD sub-images show the distinguishable but slightly overlapping frequency comb lines on the detector, originating from the two spectrograph fibers, which are both fed by the same comb. **c**, Extracted 1-dimensional comb spectra of both harmonics; the insets show a magnified (linear scale) portion of the spectrum and the 18 GHz-spaced comb lines. The UV detector cutoff is marked.

part of the poling structure, we compare in Figure 2d a waveguide poled for broadband SHG ( $\Lambda$  weakly chirped as indicated) with an unpoled waveguide (Fig. 2e), demonstrating markedly different behaviors. The poled waveguide creates a broadband SHG at approximately 400 THz, whereas the unpoled waveguide only creates narrow SHG. These observations agree with numerical simulation via

*pyChi* [64] (shown below the experimental spectra). Note that the poled waveguide also exhibits a more substantial broadening of the input spectrum (and its harmonics), which can be explained through the contributions of cascaded  $\chi^{(2)}$ -processes to the effective  $\chi^{(3)}$ -nonlinearity. In a more advanced design (Fig. 2f) a short SHG section (supporting also broadening) is followed by a longer and

strongly chirped section designed to enable FHG. Indeed pronounced FHG is visible, although, in contrast to the simulation, it is not stronger than the THG signal; we attribute this to the very small values of  $\Lambda < 2 \mu\text{m}$ , which are challenging to fabricate with high fidelity. To overcome the fabrication challenge for very small  $\Lambda$ , we also consider higher-order QPM (Fig. 2b). In higher-order QPM, the poling period is an integer multiple  $q$  of the fundamental poling period  $\Lambda$  [65], which relaxes fabrication requirements at the cost of reduced efficiency. In our design for symmetric poling (equal length for both crystal orientations),  $q$  is an odd-integer (here: 3); In addition, unintentional phase-matching may occur involving higher-order waveguide modes and coupling between orthogonal polarizations. A possible design is shown in Fig. 2g, where, after a short length of SHG poling,  $\Lambda$  ranges from 2 to 7  $\mu\text{m}$ . This choice of  $\Lambda$  respects the fabrication limit and provides QPM for most processes (Fig. 2b). The generated harmonic spectrum extends across 600 THz (ca. 350 to 1000 nm) within  $\sim 20$  dB of dynamic range, demonstrating, in agreement with previous work [52], the potential of LiNbO<sub>3</sub> waveguides for generating gap-free spectra in the VIS and UV domains.

**Spectrograph calibration.** With the principle of efficient harmonic generation validated, we build a dedicated ultraviolet astrocomb and use it for spectrograph calibration under realistic conditions at the high-resolution echelle spectrograph SOPHIE [60] at the Observatoire de Haute Provence (OHP, France). With the help of an Echelle-grating and a prism, the spectrograph cross disperses the input spectrum on a 2-dimensional charged coupled device (CCD) detector array so that the spectrum is arranged in a vertically separated set of nearly horizontal lines (*Echelle orders*), where each line represents a distinct wavelength interval. The SOPHIE spectrograph, covers the wavelengths  $\lambda$  from 387 nm to 708 nm with a resolving power of  $R = \frac{\lambda}{\Delta\lambda} \approx 75'000$  (i.e. frequency resolution of approximately 10 GHz at 400 nm wavelength) and its echelle grating is enclosed in a pressure vessel to reduce externally induced drifts. Traditionally, wavelength calibration can be obtained via thorium-argon hollow-cathode lamps (ThAr) and a passively-stabilized Fabry-Pérot etalon (FP) [66, 67], permitting calibration on the 1 to 2  $\text{m s}^{-1}$  level [68].

As an initial IR comb generator, we utilize an 18 GHz EO comb, similar to [62] (Fig. 3a). A CW laser of wavelength 1556.2 nm is stabilized to an optical resonance frequency in rubidium (Rb), providing an absolute frequency anchor for the IR EO comb (Methods). Comb generation proceeds by sending the CW laser through two electro-optic phase- and one electro-optic intensity modulator, creating an initial IR comb spanning approximately 0.6 THz. The modulation frequency of 18 GHz is provided by a low-noise microwave synthesizer, referenced to a miniature Rb atomic frequency source; over the relevant time scales of our experiments, a relative frequency

stability better than  $10^{-11}$  is achieved (Methods). In a waveshaper, a polynomial spectral phase up to 3<sup>rd</sup> order is imprinted on the EO comb spectrum, to ensure short pulses after the amplification in an erbium-doped fiber amplifier (EDFA) and an additional stretch of optical fiber for nonlinear pulse compression. In this way, an 18 GHz femtosecond pulse train with 3 W of average power can be generated. The pulses are out-coupled to free-space and coupled to the chip via a high-numerical aperture (NA=0.7) lens (estimated on chip pulse energy  $\sim 20$  pJ). Despite the high average input power levels, we did not observe any waveguide damage. For comb generation, we choose the waveguide in Fig. 2f, as it exhibits a strong UV signal and a clear separation between the harmonics. We arrange the waveshaper and the optical fiber after the amplifier such that the driving pulses are of ca. 200 fs duration, maintaining the separation between the harmonics, so that the emergence of inconsistent frequency combs, as described above, can be excluded. As we show in the SI, Section 5, shorter pulses can enable the generation of broadband and merging harmonics, which opens opportunities for future work. The generated spectra are similar to those generated at lower repetition rate (Fig. 2d-g). The chip's output, including fundamental and higher-order waveguide modes, is collimated using a parabolic mirror and sent through a tunable prism for coarse wavelength filtering and balancing of flux levels as needed, before being coupled to a multi-mode fiber. The light is sent through a mode-scrambler (see Methods) and then routed to an auxiliary input port in the spectrograph's calibration unit, which marks the interface between our LFC setup and the existing telescope and spectrograph infrastructure at OHP [60]. The calibration unit splits the comb light equally into two optical fibers (A/B fiber), which are placed next to each other on the spectrograph entrance slit, each creating an equivalent cross-dispersed spectrum on the 2-dimensional detector. Figure 3b shows a comb spectrum as recorded on the CCD detector of the SOPHIE spectrograph. The comb structure of the LFC spectrum is clearly visible along the individual spectral orders of the cross-dispersed echelle spectrograph for both A and B fibers. Data extraction and reduction of the LFC exposures is performed using a custom code initially developed for the ESPRESSO spectrograph [69]. It extracts the spectral information from the 2-dimensional detector frame using a variant of the *flat-relative optimal extraction* algorithm [70], provides default wavelength calibration based on a combined ThAr/FP wavelength solution [69, 71], and combines the data from the individual spectral orders to a single 1-dimensional spectrum (Fig. 3c) and thus makes it accessible to subsequent analysis. The resolving power of the spectrograph is not sufficient to fully separate the comb lines. In particular in the UV part of the spectrum, the wings of the spectrograph's line-spread functions for adjacent comb lines overlap and imply a reduced contrast. Nevertheless, the individual comb lines are clearly discernible.

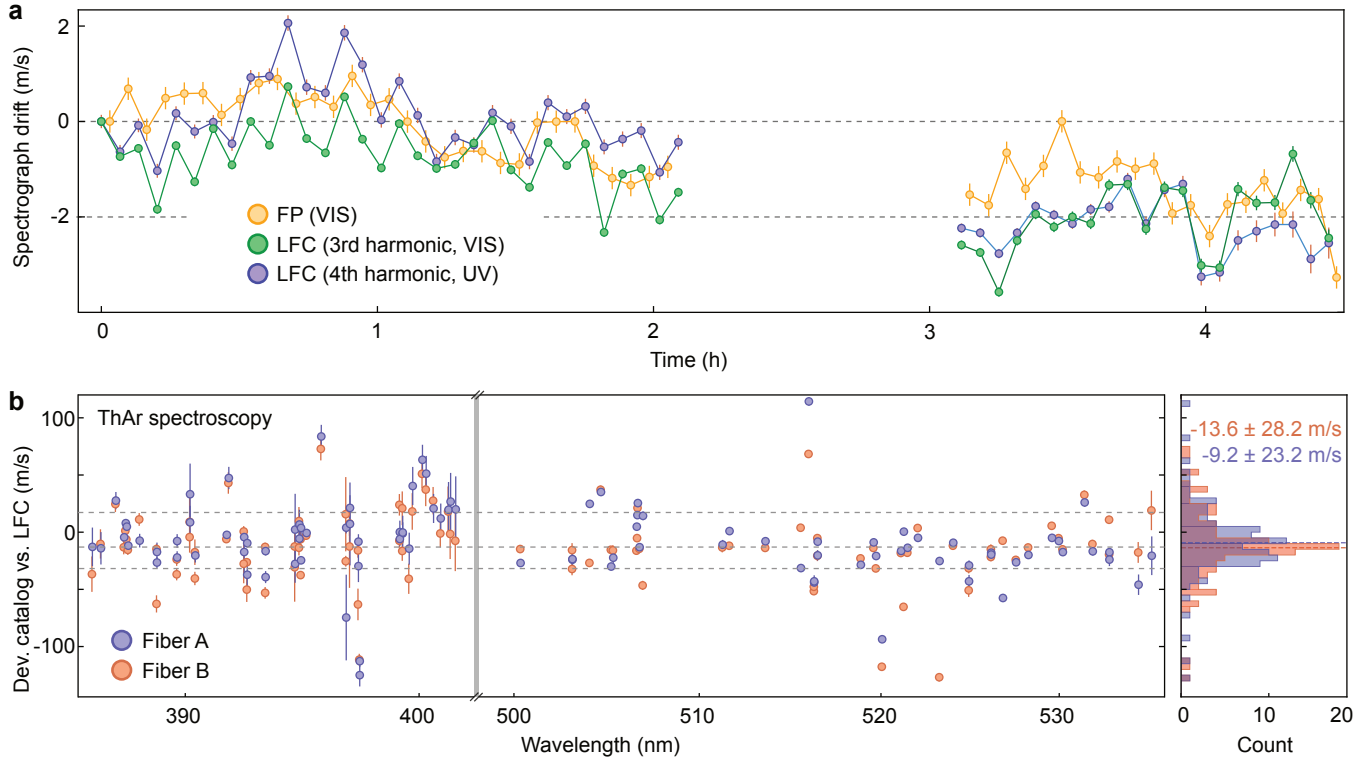


**Figure 4 | Spectrograph calibration.** **a**, Spectrograph drift measurement based on the Fabry-Pérot (FP) etalon in the visible (VIS) wavelength and the laser frequency comb (LFC) in VIS and ultraviolet (UV) wavelength range. The FP calibration data has been restricted to its spectral overlap with the VIS LFC; Error bars indicate formal uncertainties based on a propagation of photon- and read-out noise. **b**, Absolute spectroscopy of thorium emission lines by the LFC calibrated spectrograph. The deviation of the literature values from our LFC-calibrated measurement is shown as function of wavelength and separately for A and B fiber. Error bars indicate formal fitting uncertainties based on a propagation of photon- and read-out noise; dashed lines indicate 16th, 50th, and 84th percentiles. Right panel: histogram of the deviations, separated for Fiber A and B. Mean and standard deviation are indicated.

To test the *stability* of the LFC-based wavelength calibration, we obtain over several hours repeated LFC exposures interleaved with exposures of the FP etalon. The two types of exposures allow to measure the spectrograph drift in independent ways, once relative to the LFC and once relative to the FP. After data reduction as described above, all LFC lines in the spectra are fitted individually to determine their positions on the detector (Methods). For the FP exposures, the gradient method [72] is used to non-parametrically detect shifts of the spectra on the detector. As shown in Figure 4a, we obtain separate drift measurements from the 3<sup>rd</sup> and 4<sup>th</sup> harmonic and in addition one drift value from the FP, where we only use the FP lines that overlap spectrally with the 3<sup>rd</sup> harmonic (the FP calibration does not cover the UV). All three measurements agree well (within the amplitude of their scatter) and detect a systematic spectrograph drift of ca. -2 m/s over 4 hours. The agreement between the 3<sup>rd</sup> harmonic and the FP validates the LFC, and the agreement between the 4<sup>th</sup> harmonic with the two other measurements extends the validation to the UV regime. The slightly higher noise in the LFC data, i.e. remaining differences between 3<sup>rd</sup> and 4<sup>th</sup> harmonic and scatter around the global trend, compared to the FP drift measurement, can probably be attributed to a combination of effects, e.g. intrinsic sys-

tematics of the spectrograph like detector stitching issues [73] or charge transfer inefficiency (CTI) [74] combined with a change in the flux levels of the LFC lines. Moreover, the line spacing of our comb (18 GHz), which is limited by our specific technical components, is less than half the FSR of the FP calibrator (39 GHz). As a result, comb line fitting (cf. Methods) is more challenging and slightly higher scatter can be expected, when compared to the FP-based calibration. Implementing a comb with larger spacing or higher resolution spectrographs can address this challenge. The fact that nevertheless the scatter in the FP and comb-based calibrations are comparable, indicates that the obtained precision is here limited by the spectrograph, not by the comb (indeed, the scatter is consistent with the design goals of the spectrograph [60]).

To test the *accuracy* of our LFC-based calibration, we compare it to the established laboratory wavelengths of the ThAr hollow-cathode lamp. For this, two exposures, one containing the LFC and the other the ThAr spectrum, are obtained in quick succession, which ensures that no relevant spectrograph drift happens between the two exposures. In the extracted LFC spectrum, individual lines are fitted (see above and Methods) and, together with the knowledge about their true, intrinsic frequencies (Eq. 1), a purely LFC-based wavelength solution, i.e. a relation be-

tween CCD pixel position and wavelength, is derived for the spectral region covered by the comb. This LFC wavelength solution is then applied to the extracted ThAr spectrum and, after fitting of line centroids, LFC-calibrated wavelengths are assigned to the thorium lines. These are then compared to the laboratory wavelengths from [75] and the deviations are shown in Fig. 4b. The histogram of all deviations shows a global offset of  $-9$  to  $-14$  m/s with a standard deviation of  $> 20$  m/s, which is consistent with zero offset, and also with an equivalent comparison performed with the highly accurate ESPRESSO spectrograph [69]. We note that the large uncertainty (the standard deviation in the histogram) is not limited by the comb calibrator but due to the low number of only  $\sim 100$  ThAr lines that are available for comparison. The scatter of individual line deviations (and the difference between Fibers A and B), which significantly exceeds the formal uncertainties, has also been observed for other spectrographs (e.g. ESPRESSO [69]) and seems to be a common systematic, probably related to an imperfect determination of the instrumental line-spread function. We confirm that this scatter is identical when comparing thorium lines to LFC or ThAr/FP wavelength solutions [69, 71]. Therefore, we conclude that the LFC wavelength calibration is accurate to the level testable with SOPHIE. Both measurements combined validate on the proof-of-concept level that the generated astrocomb can provide precise and absolute calibration even at UV wavelengths.

**Microresonator based UV astrocombs.** Finally, we explore photonic chip-integrated microresonators (*microcombs* [23–25]) as the fundamental IR comb generator. While their current level of maturity is lower than that of EO comb generators or mode-locked lasers, microcombs can provide compact and energy efficient [76] high-repetition rate, low-noise femtosecond pulses [77], and their potential for microresonator astrocombs has already been demonstrated in the IR spectral range [26, 27]. Combined with highly efficient frequency conversion in  $\text{LiNbO}_3$  waveguides, potentially in a resonant configuration [78–80], they could open new opportunities for space-based calibrators, where energy consumption, size, and robust integration are key. Such space-based systems could calibrate ground-based observatories through the atmosphere, or provide calibration to space-based observatories, which would entirely avoid limiting atmospheric effects, such as absorption or turbulence. Therefore, as a proof-of-concept, we replace the electro-optic comb generator with a silicon nitride microresonator [81, 82] (Fig. 5c, photo) operating at  $f_{\text{rep}}=25$  GHz (Methods). A portion of the generated comb spectrum is bandpass-filtered and pre-amplified in an erbium-doped fiber amplifier (cf. Fig. 5a). Figure 5b shows the IR comb spectrum generated by the microresonator as well as the filtered and amplified spectrum. The remainder of the setup is the same as described before for the EO astrocomb (Fig. 3a). While we do not stabilize the microcomb spectra we observe broad-

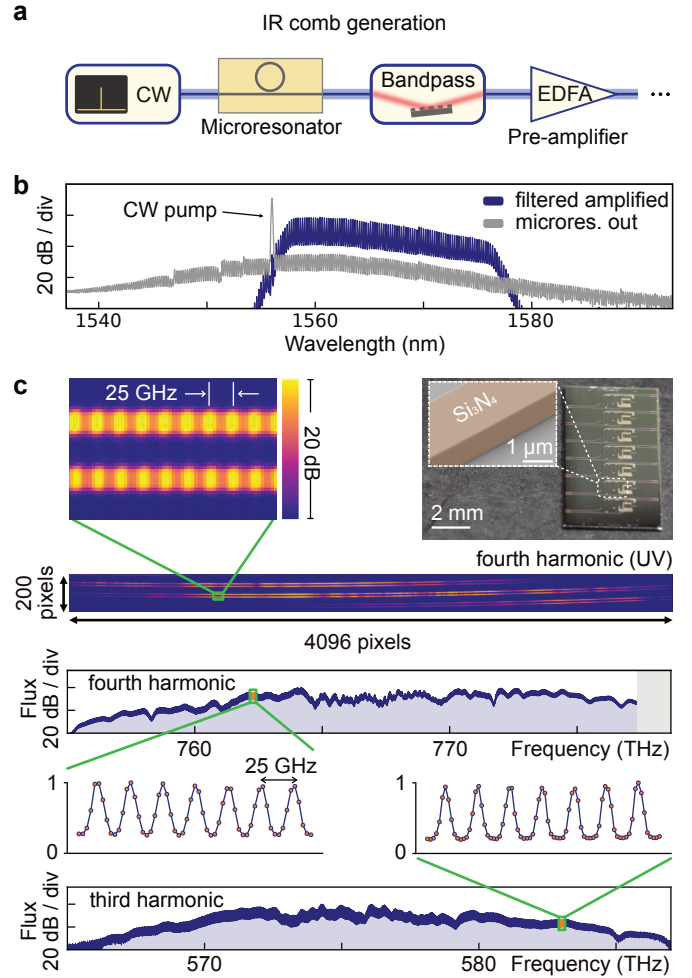


**Figure 5 | Microresonator-based ultraviolet astrocombs.** **a**, Modified setup for microresonator-based ultraviolet (UV) astrocomb generation. **b**, Microresonator comb output spectrum (gray); bandpass filtered and pre-amplified microresonator-based comb spectrum. **c**, Microresonator-based UV fourth harmonic and visible (VIS) third harmonic comb spectra, following the scheme in Fig. 3. The photo shows the photonic chip with the microresonator (dashed-line box) and the inset shows a scanning electron microscope image of the  $\text{Si}_3\text{N}_4$  resonator waveguide.

band harmonics of distinct comb lines, similar to the EO comb configuration (Fig. 5c), illustrating the potential of implementing all nonlinear optical components via highly-efficient photonic integrated circuits.

Although lithium niobate is known to show photo-induced damage by visible and ultraviolet light, we did not observe any signs of degradation in our experiments and attribute this to the relatively low flux levels in these wavelength domains (The power in the harmonics and corresponding conversion efficiencies are presented in the SI, Section 3). In a dedicated experiment, described in Section 4 of the SI, we transmitted light of a 405 nm laser diode through the waveguide and did also not observe any degradation. Zirconium-doping of the lithium niobate can further increase the damage threshold for visible and ultraviolet light [83].

## Discussion

Our results show for the first time astronomical spectrograph calibration in the UV wavelength range with a laser frequency comb. This demonstration is particularly relevant to the emerging field of optical precision cosmology with next generation instruments and telescopes. Our astrocomb’s architecture is based on periodically-poled lithium niobate nanophotonic waveguides tailored to provide efficient frequency conversion of a robust, alignment-free 18 GHz electro-optic frequency comb. Moreover, we show compatibility of the approach with photonic chip-integrated microcombs, creating opportunities for future space-based systems. This also represents the first demonstration of nonlinear transfer of a microcomb to VIS and UV wavelengths, adding new operating domains to the repertoire of these sources. The approach demonstrated here can be utilized to extend calibration beyond established wavelength ranges towards shorter wavelengths. Future work may pursue wider harmonic spectra (cf. SI, Section 5), where however, consistency of the generated spectra via suitable control of the fundamental comb’s offset-frequency (as described above) and noise suppression as previously demonstrated for electro-optic combs [63] would need to be implemented. With improved chip-coupling [47, 84] this could enable gap-free VIS and UV operation based on robust telecommunication wavelength IR lasers. Similar results may be possible also in other waveguide materials such as aluminum nitride (AlN), where broadband phase matching may be achieved through chirped geometries [85]. In addition to the development of the comb source itself, spectral flattening [86] will be needed to ensure optimal exposure of the CCD and to avoid systematic effects that can arise from strong modulation of the combs spectral envelope. In sum, the demonstrated approach opens a viable route towards astronomical precision spectroscopy in the ultraviolet based on robust infrared lasers and may eventually contribute to major scientific discoveries in cosmology and astronomy.

## Methods

**Waveguide and microresonator fabrication.** Lithium niobate waveguides for UV comb generation are fabricated from a 800 nm-thick x-cut LiNbO<sub>3</sub> layer on 3  $\mu\text{m}$  SiO<sub>2</sub> and bulk Si substrate (NANOLN). First, chromium (Cr) electrodes for periodic poling are fabricated using electron beam lithography and lift-off. Ferroelectric domain inversion is performed by applying a high-voltage waveform across the electrodes, adapted from [87] (SI, Fig. 5). After poling, the electrodes are removed via chemical etching. Waveguides are patterned using electron beam lithography on a Cr hard mask. Cr is etched using argon (Ar) ion-beam etching and subsequently, the lithium niobate layer is fully etched (no slab remaining) via reactive-ion etching with fluorine chemistry. The remaining Cr hard mask is later removed with chemical etching. Lastly, a 3  $\mu\text{m}$ -thick SiO<sub>2</sub> cladding layer is deposited using chemical vapor deposition and waveguide facets are defined by deep etching to ensure low-loss coupling to the

waveguides. More details regarding the fabrication of lithium niobate waveguides can be found in SI, Section 2. The Si<sub>3</sub>N<sub>4</sub> microresonator is designed with a finger shape [82] and fabricated via the subtractive processing method as described in ref. [81]. The height and the width of the SiN waveguide are 740 nm and 1800 nm respectively, which result in a group velocity dispersion coefficient of  $\beta_2 = -73 \text{ ps}^2/\text{km}$  for the fundamental TE mode at the pump wavelength. The total linewidth of the critically coupled resonator is 25 MHz. Lensed fibers are used for coupling into and out of the bus waveguide. More details are provided in Section 2 of the SI.

**CW laser frequency lock.** A narrow-linewidth CW laser at telecommunication wavelength 1556.2 nm (Redfern Integrated Optics, RIO Planex) is split and one part is used for EO comb generation. The other part is frequency-doubled and brought into resonance with the  $5S_{1/2}(F_g = 3) - 5D_{5/2}(F_e = 5)$  two-photon transition in <sup>85</sup>Rb atoms in a microfabricated atomic vapor cell, similar to [88]. A stable frequency lock of the CW laser to the two-photon transition is achieved by means of synchronous detection and by modulating the laser’s injection current. Using the same vapor cell and a laser with higher phase noise, we measured the fractional frequency instability of our system to an Allan deviation better than  $2 \times 10^{-12}$  for averaging times from 1 s to  $10^4$  s.

**Miniature atomic frequency source.** The 10 MHz sine wave output of a commercial miniature atomic frequency source is provided to the microwave synthesizer as a stable reference. The miniature atomic clock we use is based on a transition in the ground state of <sup>85</sup>Rb. Its relative frequency stability is specified by the manufacturer to be better than  $1 \times 10^{-10}$  ( $1 \times 10^{-11}$ ) at 1 s (100 s) averaging time; daily drift  $< 1 \times 10^{-11}$ .

**Mode scrambler and calibration unit.** The mode-scrambler suppresses detrimental laser speckles on the CCD (modal noise) that would result from the coherent LFC illumination after propagating through the multi-mode fiber train of the SOPHIE spectrograph. It consists of a rotating diffuser disc and has a throughput of  $\approx 5\%$  effectively washing out any laser speckle pattern. Averaged over one CCD exposure time, it populates all fiber modes and therefore ensures a speckle-free image of the spectrograph’s entrance aperture on the CCD. After the mode scrambler the light is guided by a multi-mode fiber to the calibration unit. The calibration unit selects one of the installed calibration light sources or, via a temporarily added additional input port, the light from the LFC. The selected light is then sent to the spectrograph’s front-end, mounted at the Cassegrain focus of the OHP 1.93 m telescope, where it is simultaneously injected into A and B fibers feeding the spectrograph [60].

**LFC line fitting and computation of drift.** The LFC lines are fitted to find their exact center positions. Due to the limited resolution of the spectrograph, the comb lines are not fully separated but partially overlap, particularly in the UV domain. Therefore, always three LFC lines are fitted together, a central line of interest and two flanking ones to model the flux contributed by their wings. In addition, the diffuse background flux is locally modeled by a polynomial of first order.

A detailed characterization of the SOPHIE instrumental line-spread function is not available. Therefore, we have to resort to model all lines with a simple Gaussian shape. In addition, due to the limited sampling (about 2.5 pixel per FWHM) on the detector, a simultaneous and unconstrained fit of all nine model parameters (positions and amplitudes of the three lines in question, one common line width, and amplitude and slope for the diffuse background) leads to degeneracies and unphysical fit results. The width of all LFC lines in the fit is therefore fixed to a FWHM of 2.47 pixels. This value was inferred from the thorium lines and, although not capturing the variation of the instrumental line-spread function along individual spectral orders or with wavelength in general, found to better describe the line shapes than a width that is fixed in velocity units.

For each exposure, the fitted line centroids are compared to the corresponding positions in the first exposure of the sequence, the differences converted to a radial velocity shifts following the Doppler formula, and then combined to provide one average drift measurement per exposure.

## Funding

This project has received funding from the Swiss National Science Foundation (Sinergia BLUVES CRSII5\_193689), the European Research Council (ERC) under the EU's Horizon 2020 research and innovation program (ERC StG 853564 and ERC CoG 771410), and through the Helmholtz Young Investigators Group VH-NG-1404; the work was supported through the Maxwell computational resources operated at DESY. The lithium niobate waveguides were fabricated in the EPFL Center of MicroNanoTechnology (CMi).

## Data availability

The datasets generated and analysed during the current study are available from the corresponding author on reasonable request.

## Code availability

The numeric simulations in the current study use an open source code available at <https://github.com/pychi-code/pychi>.

## Competing interests

We declare that none of the authors have competing interests.

## References

1. Mayor, M. & Queloz, D. A Jupiter-mass Companion to a Solar-Type Star. *Nature* **378**, 355–359 (1995).
2. Fortier, T. & Baumann, E. 20 Years of Developments in Optical Frequency Comb Technology and Applications. *Communications Physics* **2**, 1–16 (2019).
3. Diddams, S. A., Vahala, K. & Udem, T. Optical Frequency Combs: Coherently Uniting the Electromagnetic Spectrum. *Science* **369**, eaay3676 (2020).
4. Murphy, M. T. *et al.* High-Precision Wavelength Calibration of Astronomical Spectrographs with Laser Frequency Combs. *Monthly Notices of the Royal Astronomical Society* **380**, 839–847 (2007).
5. Fischer, D. A. *et al.* State of the Field: Extreme Precision Radial Velocities\*. *Publications of the Astronomical Society of the Pacific* **128**, 066001 (2016).
6. Steinmetz, T. *et al.* Laser Frequency Combs for Astronomical Observations. *Science* **321**, 1335–1337 (2008).
7. Li, C.-H. *et al.* A Laser Frequency Comb That Enables Radial Velocity Measurements with a Precision of 1 Cm S<sup>-1</sup>. *Nature* **452**, 610–612 (2008).
8. Braje, D. A., Kirchner, M. S., Osterman, S., Fortier, T. & Diddams, S. A. Astronomical Spectrograph Calibration with Broad-Spectrum Frequency Combs. *The European Physical Journal D* **48**, 57–66 (2008).
9. McCracken, R. A., Charsley, J. M. & Reid, D. T. A Decade of Astrocombs: Recent Advances in Frequency Combs for Astronomy [Invited]. *Optics Express* **25**, 15058–15078 (2017).
10. Herr, T. & McCracken, R. A. Astrocombs: Recent Advances. *IEEE Photonics Technology Letters* **31**, 1890–1893 (2019).
11. Marconi, A. *et al.* ANDES, the High Resolution Spectrograph for the ELT: Science Case, Baseline Design and Path to Construction in Ground-Based and Airborne Instrumentation for Astronomy IX **12184** (SPIE, 2022), 720–735.
12. Webb, J. K., Flambaum, V. V., Churchill, C. W., Drinkwater, M. J. & Barrow, J. D. Search for Time Variation of the Fine Structure Constant. *Physical Review Letters* **82**, 884–887 (1999).
13. Murphy, M. T. *et al.* Fundamental Physics with ESPRESSO: Precise Limit on Variations in the Fine-Structure Constant towards the Bright Quasar HE 0515-4414. *Astronomy & Astrophysics* **658**, A123 (2022).
14. Sandage, A., Véron, P. & Wyndham, J. D. Optical Identification of New Quasi-Stellar Radio Sources. *The Astrophysical Journal* **142**, 1307–1311 (1965).
15. Liske, J. *et al.* Cosmic Dynamics in the Era of Extremely Large Telescopes. *Monthly Notices of the Royal Astronomical Society* **386**, 1192–1218 (2008).
16. Cristiani, S. *et al.* Spectroscopy of QUBRICS Quasar Candidates: 1672 New Redshifts and a Golden Sample for the Sandage Test of the Redshift Drift. *Monthly Notices of the Royal Astronomical Society* **522**, 2019–2028 (2023).
17. Martins, C. J. A. P. *et al.* Cosmology and fundamental physics with the ELT-ANDES spectrograph. *arXiv e-prints*, arXiv:2311.16274. arXiv: 2311.16274 [astro-ph.CO] (2023).

18. Hirano, T. *et al.* Precision radial velocity measurements by the forward-modeling technique in the near-infrared. *PSAJ* **72**, 93. arXiv: 2007.11013 [astro-ph.EP] (2020).
19. Milaković, D. & Jethwa, P. A new method for instrumental profile reconstruction of high resolution spectrographs. *arXiv e-prints*, arXiv:2311.05240. arXiv: 2311.05240 [astro-ph.IM] (2023).
20. Benedick, A. J. *et al.* Visible Wavelength Astro-Comb. *Optics Express* **18**, 19175–19184 (2010).
21. Kashiwagi, K. *et al.* Direct Generation of 12.5-GHz-spaced Optical Frequency Comb with Ultrabroad Coverage in near-Infrared Region by Cascaded Fiber Configuration. *Optics Express* **24**, 8120–8131 (2016).
22. Yi, X. *et al.* Demonstration of a Near-IR Line-Referenced Electro-Optical Laser Frequency Comb for Precision Radial Velocity Measurements in Astronomy. *Nature Communications* **7**, 10436 (2016).
23. Kippenberg, T. J., Gaeta, A. L., Lipson, M. & Gorodetsky, M. L. Dissipative Kerr Solitons in Optical Microresonators. *Science* **361**, eaan8083 (2018).
24. Pasquazi, A. *et al.* Micro-Combs: A Novel Generation of Optical Sources. *Physics Reports. Micro-Combs: A Novel Generation of Optical Sources* **729**, 1–81 (2018).
25. Gaeta, A. L., Lipson, M. & Kippenberg, T. J. Photonic-Chip-Based Frequency Combs. *Nature Photonics* **13**, 158–169 (2019).
26. Suh, M.-G. *et al.* Searching for Exoplanets Using a Microresonator Astrocomb. *Nature Photonics* **13**, 25 (2019).
27. Obrzud, E. *et al.* A Microphotonic Astrocomb. *Nature Photonics* **13**, 31 (2019).
28. Aghanim, N. *et al.* Planck 2018 Results - VI. Cosmological Parameters. *Astronomy & Astrophysics* **641**, A6 (2020).
29. Wilken, T. *et al.* A Spectrograph for Exoplanet Observations Calibrated at the Centimetre-per-Second Level. *Nature* **485**, 611–614 (2012).
30. Phillips, D. F. *et al.* Calibration of an Astrophysical Spectrograph below 1 m/s Using a Laser Frequency Comb. *Optics Express* **20**, 13711–13726 (2012).
31. Metcalf, A. J., Fredrick, C. D., Terrien, R. C., Papp, S. B. & Diddams, S. A. 30 GHz Electro-Optic Frequency Comb Spanning 300 THz in the near Infrared and Visible. *Optics Letters* **44**, 2673–2676 (2019).
32. Glenday, A. G. *et al.* Operation of a Broadband Visible-Wavelength Astro-Comb with a High-Resolution Astrophysical Spectrograph. *Optica* **2**, 250–254 (2015).
33. McCracken, R. A. *et al.* Wavelength Calibration of a High Resolution Spectrograph with a Partially Stabilized 15-GHz Astrocomb from 550 to 890 Nm. *Optics Express* **25**, 6450–6460 (2017).
34. Wu, Y. *et al.* 20 GHz Astronomical Laser Frequency Comb with Super-Broadband Spectral Coverage in Ground-Based and Airborne Instrumentation for Astronomy IX **12184** (SPIE, 2022), 544–551.
35. Metcalf, A. J. *et al.* Stellar Spectroscopy in the Near-Infrared with a Laser Frequency Comb. *Optica* **6**, 233–239 (2019).
36. Obrzud, E. *et al.* Visible Blue-to-Red 10 GHz Frequency Comb via on-Chip Triple-Sum-Frequency Generation. *Optics Letters* **44**, 5290–5293 (2019).
37. Phillips, C. R. *et al.* Supercontinuum Generation in Quasi-Phase-Matched LiNbO<sub>3</sub> Waveguide Pumped by a Tm-doped Fiber Laser System. *Optics Letters* **36**, 3912–3914 (2011).
38. Iwakuni, K. *et al.* Generation of a Frequency Comb Spanning More than 3.6 Octaves from Ultraviolet to Mid Infrared. *Optics Letters* **41**, 3980–3983 (2016).
39. Hickstein, D. D. *et al.* High-Harmonic Generation in Periodically Poled Waveguides. *Optica* **4**, 1538–1544 (2017).
40. Rutledge, J. *et al.* Broadband Ultraviolet-Visible Frequency Combs from Cascaded High-Harmonic Generation in Quasi-Phase-Matched Waveguides. *JOSA B* **38**, 2252–2260 (2021).
41. Nakamura, K., Kashiwagi, K., Okubo, S. & Inaba, H. Erbium-Doped-Fiber-Based Broad Visible Range Frequency Comb with a 30 GHz Mode Spacing for Astronomical Applications. *Optics Express* **31**, 20274–20285 (2023).
42. Cheng, Y. S. *et al.* Continuous Ultraviolet to Blue-Green Astrocomb. *Nature Communications* **15**, 1466 (2024).
43. Desiatov, B., Shams-Ansari, A., Zhang, M., Wang, C. & Lončar, M. Ultra-Low-Loss Integrated Visible Photonics Using Thin-Film Lithium Niobate. *Optica* **6**, 380–384 (2019).
44. Honardoost, A., Abdelsalam, K. & Fathpour, S. Rejuvenating a Versatile Photonic Material: Thin-Film Lithium Niobate. *Laser & Photonics Reviews* **14**, 2000088 (2020).
45. Qi, Y. & Li, Y. Integrated Lithium Niobate Photonics. *Nanophotonics* **9**, 1287–1320 (2020).
46. Zhu, D. *et al.* Integrated Photonics on Thin-Film Lithium Niobate. *Advances in Optics and Photonics* **13**, 242–352 (2021).
47. Churaev, M. *et al.* A Heterogeneously Integrated Lithium Niobate-on-Silicon Nitride Photonic Platform 2022. arXiv: 2112.02018 [physics].
48. Brès, C.-S. *et al.* Supercontinuum in Integrated Photonics: Generation, Applications, Challenges, and Perspectives. *Nanophotonics* **12**, 1199–1244 (2023).

49. Wang, C. *et al.* Ultrahigh-Efficiency Wavelength Conversion in Nanophotonic Periodically Poled Lithium Niobate Waveguides. *Optica* **5**, 1438–1441 (2018).
50. Obrzud, E. *et al.* Stable and Compact RF-to-optical Link Using Lithium Niobate on Insulator Waveguides. *APL Photonics* **6**, 121303 (2021).
51. Park, T. *et al.* High-Efficiency Second Harmonic Generation of Blue Light on Thin-Film Lithium Niobate. *Optics Letters* **47**, 2706–2709 (2022).
52. Wu, T.-H. *et al.* Visible-to-Ultraviolet Frequency Comb Generation in Lithium Niobate Nanophotonic Waveguides. *Nature Photonics*, 1–6 (2024).
53. Chen, J.-y. *et al.* Efficient Parametric Frequency Conversion in Lithium Niobate Nanophotonic Chips. *OSA Continuum* **2**, 2914–2924 (2019).
54. Yu, M., Desiatov, B., Okawachi, Y., Gaeta, A. L. & Lončar, M. Coherent Two-Octave-Spanning Supercontinuum Generation in Lithium-Niobate Waveguides. *Optics Letters* **44**, 1222–1225 (2019).
55. Lu, J., Surya, J. B., Liu, X., Xu, Y. & Tang, H. X. Octave-Spanning Supercontinuum Generation in Nanoscale Lithium Niobate Waveguides. *Optics Letters* **44**, 1492–1495 (2019).
56. Jankowski, M. *et al.* Ultrabroadband Nonlinear Optics in Nanophotonic Periodically Poled Lithium Niobate Waveguides. *Optica* **7**, 40–46 (2020).
57. Reig Escalé, M., Kaufmann, F., Jiang, H., Pohl, D. & Grange, R. Generation of 280 THz-spanning near-Ultraviolet Light in Lithium Niobate-on-Insulator Waveguides with Sub-100 pJ Pulses. *APL Photonics* **5**, 121301 (2020).
58. Okawachi, Y. *et al.* Chip-Based Self-Referencing Using Integrated Lithium Niobate Waveguides. *Optica* **7**, 702–707 (2020).
59. Sayem, A. A. *et al.* Efficient and Tunable Blue Light Generation Using Lithium Niobate Nonlinear Photonics. *Applied Physics Letters* **119**, 231104 (2021).
60. Perruchot, S. *et al.* *The SOPHIE Spectrograph: Design and Technical Key-Points for High Throughput and High Stability in Ground-Based and Airborne Instrumentation for Astronomy II* **7014** (SPIE, 2008), 235–246.
61. Okubo, S., Onae, A., Nakamura, K., Udem, T. & Inaba, H. Offset-Free Optical Frequency Comb Self-Referencing with an f-2f Interferometer. *Optica* **5**, 188–192 (2018).
62. Obrzud, E. *et al.* Broadband Near-Infrared Astronomical Spectrometer Calibration and on-Sky Validation with an Electro-Optic Laser Frequency Comb. *Optics Express* **26**, 34830–34841 (2018).
63. Beha, K. *et al.* Electronic Synthesis of Light. *Optica* **4**, 406–411 (2017).
64. Voumard, T. *et al.* Simulating Supercontinua from Mixed and Cascaded Nonlinearities — <https://github.com/pychi-code/pychi>. *APL Photonics* **8**, 036114 (2023).
65. Suhara, T. & Nishihara, H. Theoretical Analysis of Waveguide Second-Harmonic Generation Phase Matched with Uniform and Chirped Gratings. *IEEE Journal of Quantum Electronics* **26**, 1265–1276 (1990).
66. Wildi, F., Pepe, F., Chazelas, B., Curto, G. L. & Lovis, C. *A Fabry-Perot Calibrator of the HARPS Radial Velocity Spectrograph: Performance Report in Ground-Based and Airborne Instrumentation for Astronomy III* **7735** (SPIE, 2010), 1853–1863.
67. Wildi, F., Chazelas, B. & Pepe, F. *A Passive Cost-Effective Solution for the High Accuracy Wavelength Calibration of Radial Velocity Spectrographs in Ground-Based and Airborne Instrumentation for Astronomy IV* **8446** (SPIE, 2012), 1122–1129.
68. Bouchy, F. *et al.* SOPHIE+: First Results of an Octagonal-Section Fiber for High-Precision Radial Velocity Measurements. *Astronomy & Astrophysics* **549**, A49 (2013).
69. Schmidt, T. M. *et al.* Fundamental Physics with ESPRESSO: Towards an Accurate Wavelength Calibration for a Precision Test of the Fine-Structure Constant. *Astronomy & Astrophysics* **646**, A144 (2021).
70. Zechmeister, M., Anglada-Escudé, G. & Reiners, A. Flat-Relative Optimal Extraction - A Quick and Efficient Algorithm for Stabilised Spectrographs. *Astronomy & Astrophysics* **561**, A59 (2014).
71. Cersullo, F., Coffinet, A., Chazelas, B., Lovis, C. & Pepe, F. New Wavelength Calibration for Echelle Spectrographs Using Fabry-Pérot Etalons. *Astronomy & Astrophysics* **624**, A122 (2019).
72. Bouchy, F., Pepe, F. & Queloz, D. Fundamental Photon Noise Limit to Radial Velocity Measurements. *Astronomy & Astrophysics* **374**, 733–739 (2001).
73. Coffinet, A., Lovis, C., Dumusque, X. & Pepe, F. New Wavelength Calibration of the HARPS Spectrograph. *Astronomy & Astrophysics* **629**, A27 (2019).
74. Bouchy, F. *et al.* Charge Transfer Inefficiency Effect for High-Precision Radial Velocity Measurements. *EAS Publications Series* **37**, 247–253 (2009).
75. Redman, S. L., Nave, G. & Sansonetti, C. J. THE SPECTRUM OF THORIUM FROM 250 Nm TO 5500 Nm: RITZ WAVELENGTHS AND OPTIMIZED ENERGY LEVELS. *The Astrophysical Journal Supplement Series* **211**, 4 (2014).
76. Helgason, Ó. B. *et al.* *Power-Efficient Soliton Microcombs 2022*. arXiv: 2202.09410 [physics].
77. Herr, T. *et al.* Temporal Solitons in Optical Microresonators. *Nature Photonics* **8**, 145–152 (2014).

78. Herr, S. J. *et al.* Frequency Comb Up- and down-Conversion in Synchronously Driven  $\chi^{(2)}$  Optical Microresonators. *Optics Letters* **43**, 5745–5748 (2018).
79. Jankowski, M., Mishra, J. & Fejer, M. M. Dispersion-Engineered Nanophotonics: A Flexible Tool for Non-classical Light. *Journal of Physics: Photonics* **3**, 042005 (2021).
80. Roy, A. *et al.* *Visible-to-Mid-IR Tunable Frequency Comb in Nanophotonics 2022*. arXiv: 2212.08723 [physics].
81. Ye, Z., Twayana, K., Andrekson, P. A. & Torres-Company, V. High-Q  $\text{Si}_3\text{N}_4$  Microresonators Based on a Subtractive Processing for Kerr Nonlinear Optics. *Optics Express* **27**, 35719–35727 (2019).
82. Ye, Z. *et al.* Integrated, Ultra-Compact High-Q Silicon Nitride Microresonators for Low-Repetition-Rate Soliton Microcombs. *Laser & Photonics Reviews* **16**, 2100147 (2022).
83. Liu, F. *et al.* High Resistance against Ultraviolet Photorefractive in Zirconium-Doped Lithium Niobate Crystals. *Optics Letters* **35**, 10–12 (2010).
84. He, L. *et al.* Low-Loss Fiber-to-Chip Interface for Lithium Niobate Photonic Integrated Circuits. *Optics Letters* **44**, 2314–2317 (2019).
85. Liu, X. *et al.* Beyond 100 THz-spanning Ultraviolet Frequency Combs in a Non-Centrosymmetric Crystalline Waveguide. *Nature Communications* **10**, 2971 (2019).
86. Probst, R. A. *et al.* *A Laser Frequency Comb Featuring Sub-Cm/s Precision for Routine Operation on HARPS in Ground-Based and Airborne Instrumentation for Astronomy V* **9147** (SPIE, 2014), 498–509.
87. Younesi, M. *et al.* Periodic poling with a micrometer-range period in thin-film lithium niobate on insulator. *JOSA B* **38**. Publisher: Optica Publishing Group, 685–691 (2021).
88. Newman, Z. L. *et al.* High-Performance, Compact Optical Standard. *Optics Letters* **46**, 4702–4705 (2021).

# Ultraviolet astronomical spectrograph calibration with laser frequency combs from nanophotonic lithium niobate waveguides

## Supplementary Information

Markus Ludwig,<sup>1,\*</sup> Furkan Ayhan,<sup>2,\*</sup> Tobias M. Schmidt,<sup>3,\*</sup>

Thibault Wildi,<sup>1</sup> Thibault Voumard,<sup>1</sup> Roman Blum,<sup>4</sup> Zhichao Ye,<sup>5</sup> Fuchuan Lei,<sup>5</sup>

François Wildi,<sup>3</sup> Francesco Pepe,<sup>3</sup> Mahmoud A. Gaafar,<sup>1</sup> Ewelina Obrzud,<sup>4</sup> Davide Grassani,<sup>4</sup> Olivia Hefti,<sup>4</sup> Sylvain Karlen,<sup>4</sup> Steve Lecomte,<sup>4</sup> François Moreau,<sup>6</sup> Bruno Chazelas,<sup>3</sup> Rico Sottile,<sup>6</sup> Victor Torres-Company,<sup>5</sup> Victor Brasch,<sup>7</sup> Luis G. Villanueva,<sup>2</sup> François Bouchy,<sup>3</sup> Tobias Herr<sup>1,8,\*\*</sup>

<sup>1</sup>Deutsches Elektronen-Synchrotron DESY, Notkestr. 85, 22607 Hamburg, Germany

<sup>2</sup>École Polytechnique Fédérale de Lausanne (EPFL), 1015 Lausanne, Switzerland

<sup>3</sup> Observatoire de Genève, Département d'Astronomie, Université de Genève, Chemin Pegasi 51b, 1290 Versoix, Switzerland

<sup>4</sup> Swiss Center for Electronics and Microtechnology (CSEM), 2000 Neuchâtel, Switzerland

<sup>5</sup> Department of Microtechnology and Nanoscience, Chalmers University of Technology, 41296 Gothenburg, Sweden

<sup>6</sup> Observatoire de Haute-Provence, CNRS, Université d'Aix-Marseille, 04870 Saint-Michel-l'Observatoire, France

<sup>7</sup> Q.ANT GmbH, Handwerkstraße 29, 70565 Stuttgart, Germany

<sup>8</sup>Physics Department, Universität Hamburg UHH, Luruper Chaussee 149, 22607 Hamburg, Germany

\*These authors contributed equally.

\*\*tobias.herr@desy.de

## 1 Linewidth and background in the harmonic frequency comb

The lineshape of a comb line is defined by its phase noise spectrum. Phase noise may broaden the linewidth or may contribute to a broadband background signal. Both linewidth and background have important implications for astrocombs and are discussed below.

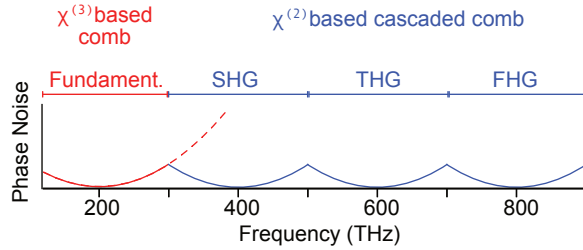
### 1.1 Phase noise and comb lineshape

Both  $\nu_0$  and  $f_{\text{rep}}$ , which are the defining frequencies of the comb (Eq. 1, main text), exhibit non-zero phase noise described by their (single-sided) phase noise power spectral densities (PSDs)  $S_{\phi}^{\nu_0}(f)$  and  $S_{\phi}^{f_{\text{rep}}}(f)$ , where  $f$  is the offset frequency from the respective carrier wave. The resulting phase noise of the comb lines is

$$S_{\phi}^{\nu_{m,n}} = m^2 S_{\phi}^{\nu_0} + n^2 S_{\phi}^{f_{\text{rep}}}, \quad (3)$$

where  $m = 1, 2, \dots$  indicates the harmonic and  $n = \pm 1, \pm 2, \dots$  the line index relative to the center of the harmonic. The second term usually limits the useful span (i.e., a maximal  $|n|$ ) of an electro-optic comb generator. To increase the useful span, noise-filtering can be applied to suppress the emergence of a strong background signal as well as linewidth broadening [1].

Creating broadband comb spectra via cascaded  $\chi^{(2)}$ -harmonics, rather than  $\chi^{(3)}$ -based broadening around  $\nu_0$ , shows distinct noise properties as frequencies  $\nu$  much higher than  $\nu_0$  can be reached through lines in a harmonic  $m$  while keeping  $n \ll (\nu_{m,n} - \nu_0)/f_{\text{rep}}$ . Neglecting the small impact of  $m^2 S_{\phi}^{\nu_0}$  (as  $m \ll n$ ), the phase noise of comb lines of frequency  $\nu_{m,n}$  that are part of the  $m^{\text{th}}$  harmonic comb does not grow in function of their frequency difference from  $\nu_0$ , but only with their distance from the  $m^{\text{th}}$  harmonics center frequency  $\nu_{m,0}$ . This permits generating UV astrocombs in a limited span around the fourth harmonic center frequencies  $\nu_{4,0}$  from a near-infrared electro-optic



**Supplementary Figure 1** | Phase noise in a traditional  $\chi^{(3)}$ -based comb compared to the phase noise a  $\chi^{(2)}$ -based comb generated through cascaded harmonics..

comb generator without noise-filtering; wider spectra around the harmonics will still require noise filtering. The different noise properties of  $\chi^{(2)}$  and  $\chi^{(3)}$ -based spectra are illustrated in Supplementary Fig. 1.

Based on the phase noise  $S_{\phi}^{f_{\text{rep}}}$  we can (numerically) estimate the lineshape  $S_n(\nu_{\text{rel}})$  of a comb line that is  $n$  lines away from the center of the harmonic by computing the Fourier transform ( $\nu_{\text{rel}}$  is the optical frequency relative to the center of the optical line)

$$S_n(\nu_{\text{rel}}) = 2 \int_{-\infty}^{\infty} \Gamma(\tau) \exp[-i2\pi\nu_{\text{rel}}\tau] d\tau \quad (4)$$

of the normalized autocorrelation function [2]

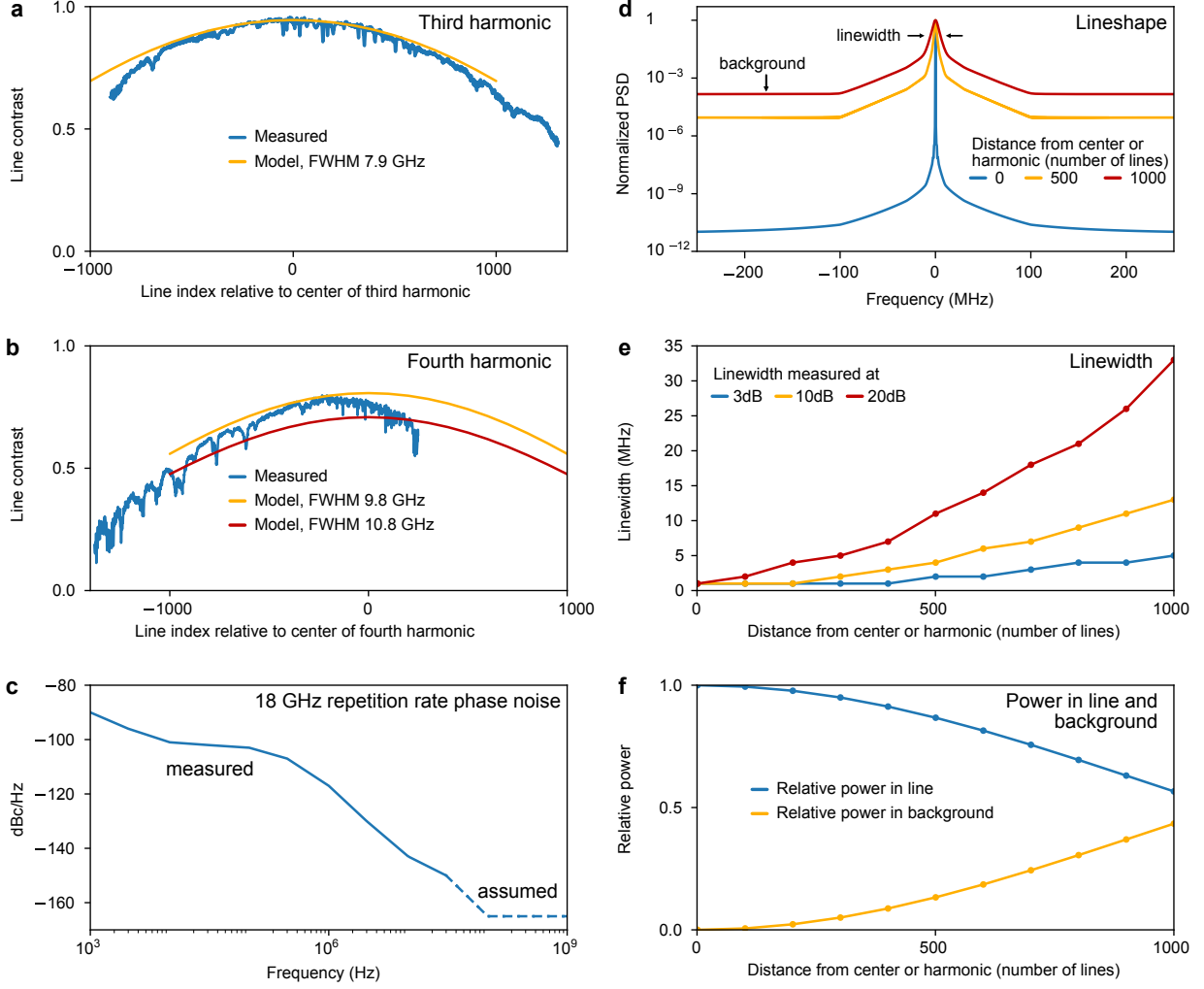
$$\Gamma(\tau) = \exp \left[ -2 \int_0^{\infty} n^2 S_{\phi}^{f_{\text{rep}}}(f) \sin^2(\pi f \tau) df \right]. \quad (5)$$

## 1.2 Experimental observation of line contrast and comparison with numeric model

An astronomical spectrograph cannot resolve the lineshapes of the comb lines but instead observes the convolution of the comb spectrum with the spectrograph's instrumental line-spread function (LSF). Depending on the lineshape of the comb lines (linewidth and background), the spacing of the comb lines and the LSF, comb lines may be observed by the spectrograph with a reduced level of contrast. Based on the discussion in Supplementary Section 1.1 one would expect that the observed line contrast reduces for larger  $|n|$  due to the increase of phase noise (causing increased background and linewidth). This is indeed observed in the experimental data. Supplementary Figure 2a,b, shows the line contrast (extracted from main text Figure 3 as the peak-valley difference divided by the peak height) in dependence of the line index  $n$  relative to the spectral centers of the third and fourth harmonics. As expected, the contrast is highest in the center of the harmonics and decreases with spectral distance from the harmonic center. Under the assumption that in the center of the harmonics the lines are narrow and there is negligible background, we can estimate the full-width-at-half maximum (FWHM) of the instrumental line-spread function which we assume to be of Gaussian shape. We find  $\approx 7.9$  GHz for the FWHM in the spectral region of the third harmonic and 9.8 GHz to 10.8 GHz in the spectral region of the fourth harmonic. Assuming that the PSD of the repetition rate phase noise can be approximated at noise frequencies up to 30 MHz by the phase noise of our microwave synthesizer and above 30 MHz exhibits a white phase noise floor of  $-165$  dBc/Hz (see 2c), we derive the lineshapes according to Supplementary Section 1.1 and perform the convolution with the estimated instrumental line-spread functions. These model results are overlaid in the Supplementary Figure 2a,b and show good qualitative agreement with the observed data. For clarity we note that the experimental noise floor in  $S_{\phi}^{f_{\text{rep}}}$  may not only stem from the microwave source but also emerge from amplified spontaneous emission (ASE) in the erbium-doped fiber amplifiers or other noise sources. To better illustrate the underlying comb lineshapes (prior to convolution), Supplementary Figure 2d shows their characteristic shapes for different values of  $n$ . Panels e and f show the linewidth at different levels as well as the relative power contained in the narrow line and in the flat background as function of  $n$ . The background power is determined by multiplying the background level in the optical PSD with the comb line spacing  $f_{\text{rep}}$ . Subtracting the background power from the total power yields the line power.

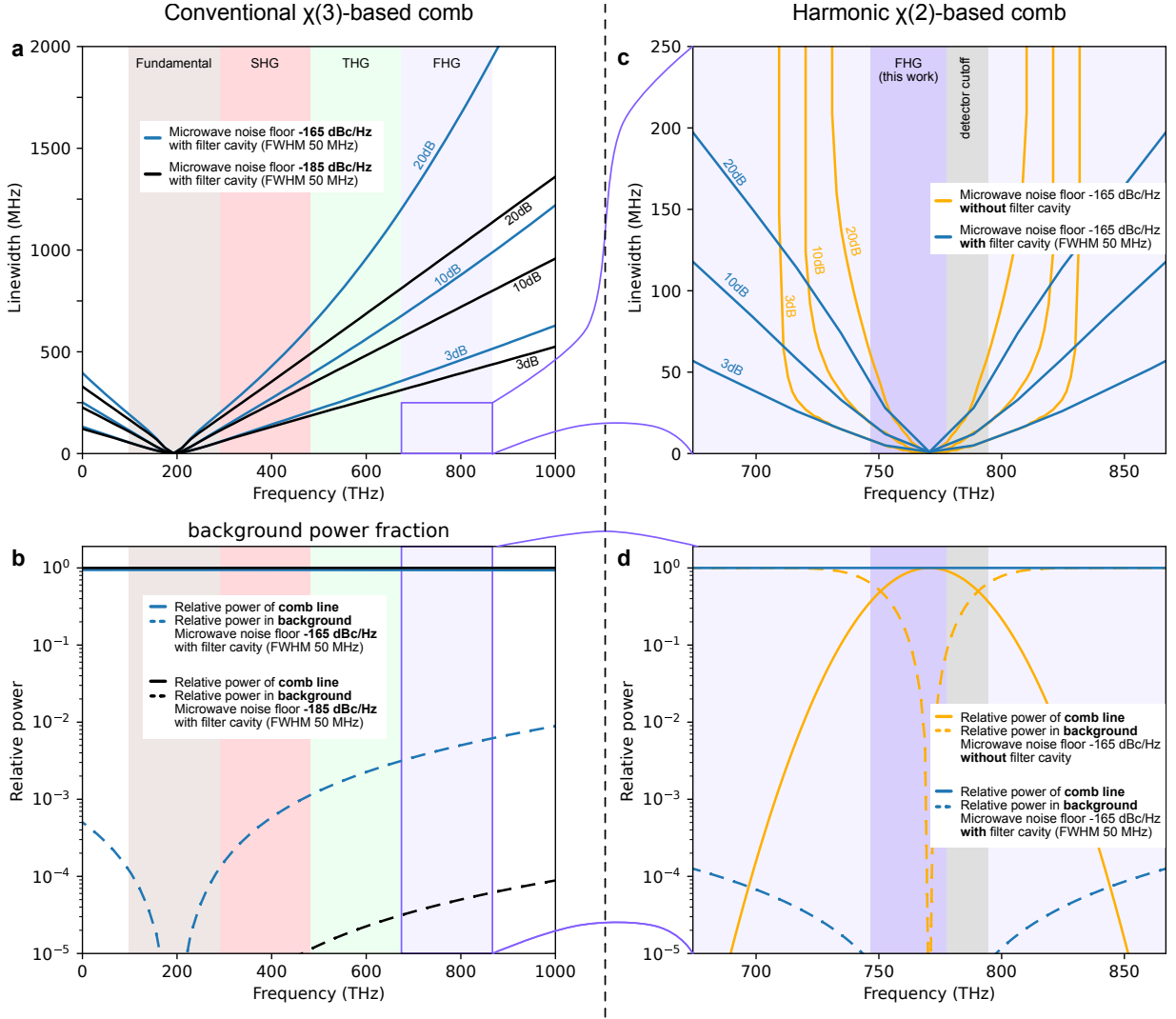
## 1.3 Comparison of linewidth and line/background power in $\chi^{(2)}$ - and $\chi^{(3)}$ -based combs

To provide additional information, also with regard to future implementations of UV electro-optic astrocombs, we have added a detailed comparison of  $\chi^{(2)}$ - and  $\chi^{(3)}$ -based comb generation in Supplementary Figure 3. This figure shows in the left column (panels a,b) the conventional  $\chi^{(3)}$ -based approach and in the right column (panels c,d) the approach based on  $\chi^{(2)}$  processes. In both cases we assume the repetition rate phase noise as shown in Figure 2c, where for the



**Supplementary Figure 2 | Contrast and lineshape.** **a**, Measured line contrast of the third harmonic and predicted contrast based on the model described in the text for an instrumental line-spread function with a full-width-at-half-maximum (FWHM) of 7.9 GHz. **b**, Same as in panel a, however, for the fourth harmonic and assuming an instrumental line-spread function with FWHM of 9.8 GHz and 10.8 GHz. **c**, Power spectral density  $S_{\phi}^{f_{\text{rep}}}$  of the repetition rate phase noise for our model, based on the measured phase noise of the microwave synthesizer driving the electro-optic comb up to 30 MHz frequency and assumed phase noise above 30 MHz (see text for details). **d**, Comb lineshape (normalized PSD) for the phase noise in panel c for different distances from the center of a harmonic. **e**, 3dB, 10dB and 20dB linewidth of the comb lines in dependence of their distance from the center of a harmonic. **f**, Relative power contained in the comb line and in the flat background (see text for details) in dependence of their distance from the center of a harmonic.

$\chi^{(3)}$ -based approach we also show a scenario with a noise floor at  $-185$  dBc/Hz (such low noise floor could be achieved when the synthesizer outputs at least 11 dBm of microwave power (thermal noise floor at  $-174$  dBm/Hz); higher power is needed when additional noise, e.g. from microwave amplification, is relevant). As a comparison between panels a and c shows, the width of the comb lines generated in the  $\chi^{(2)}$ -based approach can be well below those generated in a  $\chi^{(3)}$ -based approach. Over the wavelength range utilized in our work, and with the parameters assumed here, the  $\chi^{(2)}$ -generated lines, even without noise suppression, are expected to be narrower than those one would expect from a  $\chi^{(3)}$ -based approach with a noise suppression filter (Here we assume a noise filter of 50 MHz width). Figure 3 panels b and c compare the relative power that is contained in the line and in the flat background. The spectral interval utilized in our work is highlighted in panels c and d, indicating a sufficiently low contribution of the background so that the comb lines can be observed. Noise filtering can provide effective means of suppressing the background flux both for the  $\chi^{(3)}$ -based approach as well as for extending the  $\chi^{(2)}$ -based approach to wider bandwidth.



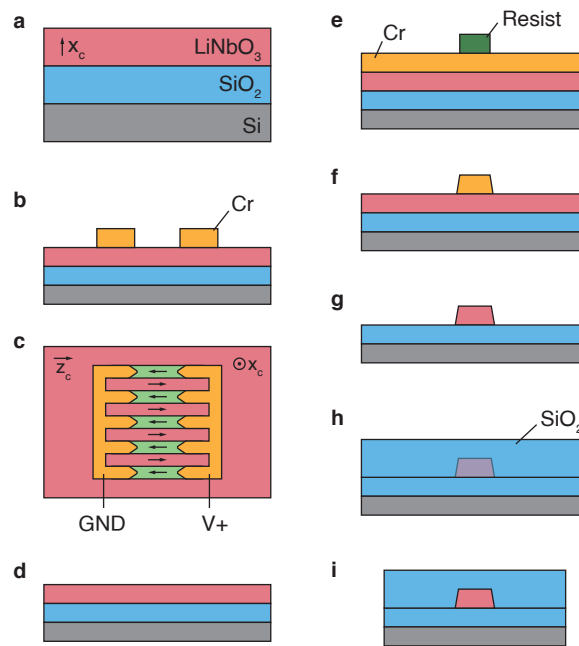
**Supplementary Figure 3** | Comparison of key characteristics in  $\chi^{(2)}$ - and  $\chi^{(3)}$ -based electro-optic combs, **a**, 3dB, 10dB and 20dB linewidth for a  $\chi^{(3)}$ -based electro-optic comb with cavity noise suppression (Full-width-at-half-maximum, FWHM, 50 MHz). The microwave phase noise is assumed to be as in Supplementary Figure 2 with a noise floor of  $-165$  dBc/Hz and  $-185$  dBc/Hz, respectively. The color-coded background indicates the spectral domains of fundamental comb, second, third and fourth harmonic generation (SHG, THG, FHG) **b**, Relative power in the flat background and in the comb line for the conditions as in panel a. **c**, 3dB, 10dB and 20dB linewidth for a  $\chi^{(2)}$ -based electro-optic comb around the center of the fourth harmonic with and without a noise filter cavity and a microwave phase noise floor of  $-165$  dBc/Hz. The spectral range used in this work and the detector cutoff are indicated. **d**, Relative power in the flat background and in the comb line for the conditions as in panel c.

## 2 Fabrication of periodically-poled lithium niobate waveguides

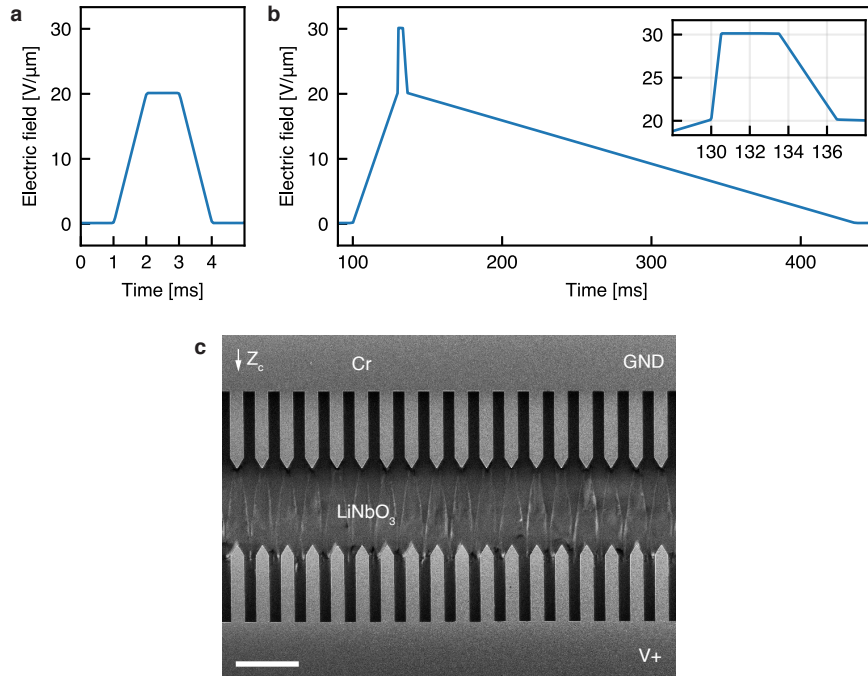
Lithium niobate waveguides for UV comb generation are fabricated on 16-by-16 mm<sup>2</sup> chips diced from a 100 mm wafer (NANOLN) with 800 nm-thick x-cut LiNbO<sub>3</sub> layer on 3  $\mu$ m SiO<sub>2</sub> and bulk Si substrate (Supplementary Figure 4a). To ensure precise alignment of the waveguides and poling electrodes in subsequent lithography steps to the crystal axes of the lithium niobate, platinum (Pt) alignment marks are patterned on wafer scale before dicing. This is done with electron-beam lithography (EBL), electron-beam evaporation (EBE) and a lift-off process.

First, chromium (Cr) poling electrodes are patterned via EBL, EBE and lift-off using MMA/PMMA bilayer resist (Supplementary Figure 4b). Electrodes are patterned such that the applied electric field across the electrodes is along the z-axis of lithium niobate (Supplementary Figure 4c). Ferroelectric domain inversion is performed by applying a high-voltage (HV) field across the electrodes in two stages: First, a *pre-poling* signal is repeated three times to help nucleation of domains closer to positive (V+) electrode (Supplementary Figure 5a). Secondly, a higher field (30 V/ $\mu$ m), followed by a slow decay is applied to propagate the initiated domains to the ground (GND) electrode (Supplementary Figure 5b). After poling, samples are inspected under a scanning electron microscope (SEM) (Supplementary Figure

5c) before removing the electrodes with wet etching (Supplementary Figure 4d). Before waveguide fabrication, a Cr layer is deposited using EBE to be used as a hard mask for etching lithium niobate. Later, waveguides are patterned with EBL (Supplementary Figure 4e). The Cr hard mask is etched using argon (Ar) ion-beam etching (IBE) (Supplementary Figure 4f). Subsequently, the lithium niobate layer is fully etched with reactive-ion etching (RIE) with fluorine chemistry ( $\text{CHF}_3/\text{Ar}$ ) (Supplementary Figure 4g). After etching, the remaining Cr hard mask is removed and the structures are cleaned with wet etching. Lastly, samples are cladded with a 3  $\mu\text{m}$ -thick  $\text{SiO}_2$  layer, deposited via chemical vapor deposition (CVD) (Supplementary Figure 4h). Finally, waveguide facets are defined by deep etching of  $\text{SiO}_2$ ,  $\text{LiNbO}_3$  and Si layers to ensure better coupling to the waveguides.



**Supplementary Figure 4 | Fabrication of periodically-poled lithium niobate waveguides.** **a**, LNOI substrate with 800 nm x-cut  $\text{LiNbO}_3$ , 3  $\mu\text{m}$   $\text{SiO}_2$  and bulk Si. **b**, Deposition of Cr electrodes for periodic poling with electron-beam lithography, electron-beam evaporation and lift-off. **c**, Periodic poling with a high-voltage source. Sample is illustrated from top. **d**, Removal of the Cr electrodes after periodic poling. **e**, Cr hard mask deposition with electron-beam evaporation and patterning of the waveguides with electron-beam lithography. **f**, Ar ion-beam etching of the Cr hard mask. **g**, Fluorine reactive-ion etching of the  $\text{LiNbO}_3$ . **h**,  $\text{SiO}_2$  cladding deposition with chemical vapor deposition. **i**, Series of reactive ion etching steps to etch  $\text{SiO}_2$ ,  $\text{LiNbO}_3$  and Si layers to reveal waveguide facets.



**Supplementary Figure 5 | Periodic poling of the lithium niobate waveguides.** **a**, One of three high-voltage *pre-poling* signals applied to electrodes for periodic poling. **b**, High-voltage *main* signal applied for poling. Inset shows the detailed section of the peak poling signal. **c**, SEM image of the poled lithium niobate sample. Scale bar is 10  $\mu\text{m}$ .

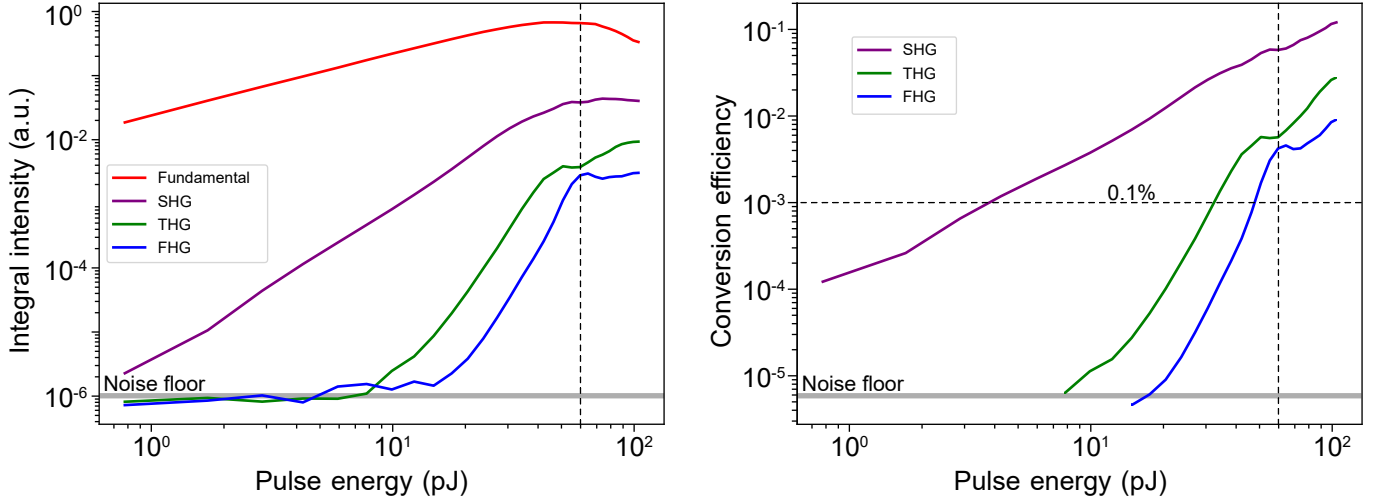
### 3 Power consumption and nonlinear conversion efficiency

#### 3.1 Power consumption

The energy consumption of the electro-optic comb generator is dominated by the multi-W erbium-doped fiber amplifier (EDFA) and the microwave electronics. Assuming a 10% wall-plug efficiency the EDFA will approximately consume 35 W of electrical power. The microwave synthesizer consumes under maximal load, depending on the specific hardware, ca. 80-130 W of electrical power, the microwave amplifiers jointly ca. 50 W of electrical power. In sum this amounts to approximately 200 W of electrical power consumption, about the same as a standard desktop computer. In case of the microresonator-based approach, one can subtract the power consumption of the microwave source and microwave amplifier, resulting in a power consumption of approximately 35 W. The power consumption of our mode-locked laser is below 15 W. However, considering the  $\sim 200$ -times lower repetition rate, the energy consumption per pulse is not better than of the electro-optic comb, although it reaches higher per pulse energy.

#### 3.2 Nonlinear conversion efficiency

To derive the conversion efficiency of the fundamental comb into the harmonics, the experimental spectra shown in Figure 2g in the main text complemented by additional spectra at different pulse energies were integrated over the respective spectral ranges of the harmonic orders. The left panel of Supplementary Figure 6 shows the resulting output power levels of the fundamental and the harmonics up to the fourth order as a function of on-chip input pulse energy. The log-log scale clearly reveals that the slopes increase with harmonic order. Consistently, also the pulse energy threshold to cross the noise floor of the spectrum analyzer increases with the harmonic order. The fact that the power in the fundamental saturates beyond 40 pJ and eventually even drops can be attributed both to an increasing depletion into the harmonics and additional spectral broadening of the fundamental which eventually exceeds the range detected by the spectrum analyzer (1750 nm). The right panel of Supplementary Figure 6 shows the conversion efficiency, i.e., the ratio of the power contained in the respective harmonic orders vs. the power in the fundamental comb. A conversion efficiency well exceeding 0.1 % is achieved for the fourth harmonic.



**Supplementary Figure 6 | Conversion efficiencies of the fundamental spectrum into the harmonics.** **Left:** Integrated intensity contained in the Fundamental spectral domain and the domains of second, third and fourth harmonic generation (SHG THG FHG). The vertical dashed line indicates a maximum on-chip input pulse energy of roughly 60 pJ beyond which the power in the fourth harmonic saturates. **Right:** Corresponding conversion efficiency.

## 4 UV irradiation test of a lithium niobate waveguide

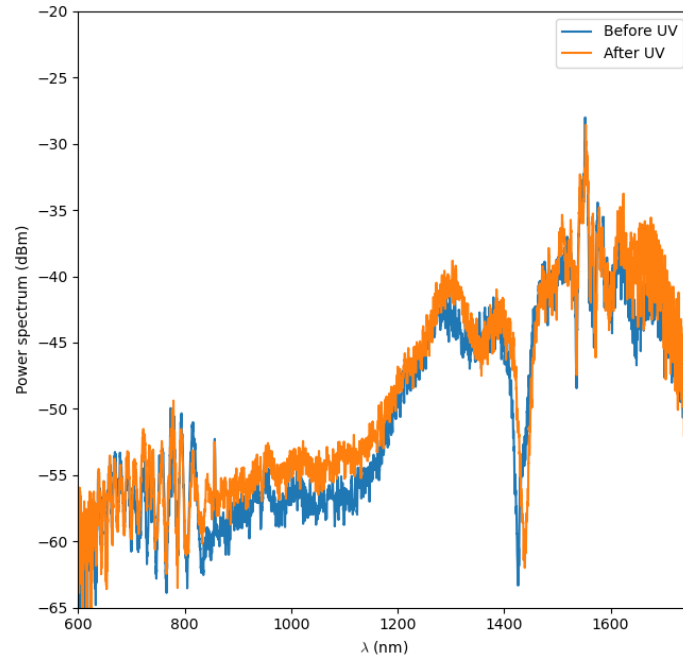
To assess the susceptibility of our waveguides to UV-induced damage, we performed an additional test, where we coupled a 405 nm laser diode to a lithium niobate waveguide (1-1.5 mW of coupled power). To perform this test, we fabricated dedicated lithium niobate waveguides that are not straight but have an S-bend on the waveguide such that input and output are offset from each other (i.e. offset in the direction orthogonal to the direction of the incoming light). This configuration enables accurate measurements of the coupled intensities without picking up stray light that has not propagated through the waveguide. Moreover, a narrow waveguide with a width of 600 nm was chosen to enhance the intensity. Over 12 hours we delivered more than 60 J optical energy through the waveguide, which would correspond to more than one week of UV exposure in astrocomb operation (assuming a UV power level of 100  $\mu$ W). We did not observe a noticeable degradation of the UV or infrared transmission through the waveguide within the precision of the measurement. Although the test waveguides were unpoled and would hence not have been suitable for spectrograph calibration, we also performed a supercontinuum generation experiment before and after UV irradiation resulting essentially in the same spectra, as shown in Supplementary Figure 7.

## 5 Broadband spectrum

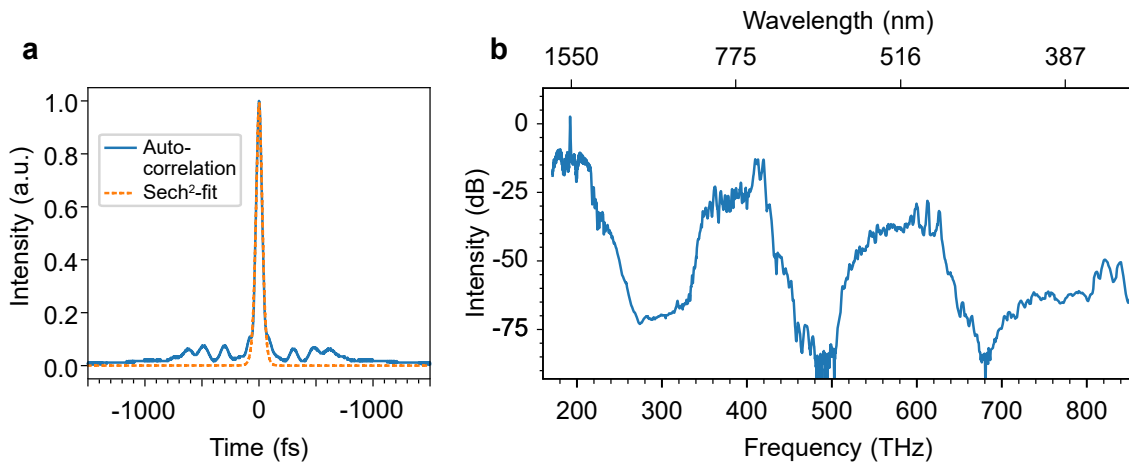
To explore the potential of extending the spectral coverage in future work, we configure the 18 GHz electro-optic comb to provide a broadband pulse with an auto-correlation trace as in Figure 8a. This is achieved via a combination of highly-nonlinear bandwidth generating fiber and compression fiber, similar to [3]. With this input pulse we generate the broadband spectrum of overlapping harmonics as shown in Figure 8b.

## References

- Beha, K. *et al.* Electronic Synthesis of Light. *Optica* **4**, 406–411 (2017).
- Domenico, G. D., Schilt, S. & Thomann, P. Simple Approach to the Relation between Laser Frequency Noise and Laser Line Shape. *Applied Optics* **49**, 4801–4807 (2010).
- Obrzud, E. *et al.* Broadband Near-Infrared Astronomical Spectrometer Calibration and on-Sky Validation with an Electro-Optic Laser Frequency Comb. *Optics Express* **26**, 34830–34841 (2018).



**Supplementary Figure 7 | Supercontinuum before and after UV irradiation.** Spectrum of a supercontinuum generated in the lithium niobate waveguide before (blue) and after (orange) UV irradiation. The mode-locked laser driving the supercontinuum has an average power of 73 mW, a pulse duration of 125 fs and repetition rate of 40 MHz.



**Supplementary Figure 8 | Broadband spectrum of an 18 GHz comb.** **a**, Auto-correlation trace and pulse duration based on a sech<sup>2</sup>-fit, retrieving a pulse duration of 38 fs (full width at half maximum of the intensity transient). **b**, Resulting spectrum with overlapping harmonics recorded on a grating based optical spectrum analyzer (OSA, model Yokogawa AQ6374).